September, 1968

REPORT ESL-R-370
M.I.T. DSR PROJECT 76343
NASA Research Grant (NsG-234-61)

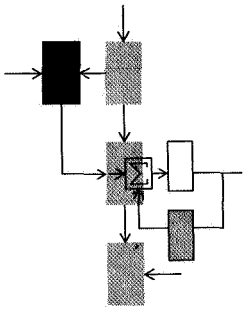

X-BAND SCATTERING MEASUREMENTS OF EARTH SURFACES FROM AN AIRCRAFT

J. F. Reintjes
J. R. Sandison
J. A. Bosco
L. W. Counts

Electronic Systems Laboratory

MASSACHUSETTS INSTITUTE OF TECHNOLOGY, CAMBRIDGE, MASSACHUSETTS 021

Department of Electrical Engineering

September, 1968 Report ESL-R-370 Copy 37

X-BAND SCATTERING MEASUREMENTS OF EARTH SURFACES FROM AN AIRCRAFT

by

J. F. Reintjes
J. R. Sandison
J. A. Bosco
L. W. Counts

The preparation and publication of this report, including the research on which it is based, was sponsored by the National Aeronautics and Space Administration under Research Grant No. NsG-234-61, M.I.T. DSR Project 76343. This report is published for information purposes only and does not represent recommendations or conclusions of the sponsoring agency. Reproduction in whole or in part is permitted for any purpose of the United States Government.

Electronic Systems Laboratory
Department of Electrical Engineering
Massachusetts Institute of Technology
Cambridge, Massachusetts 02139

ABSTRACT

An airborne radar-type instrument has been used to measure the backscattering properties of Earth surfaces at three different angles of illumination. The data obtained are used in an effort to discern a relationship between the radar-backscatter characteristics with gross surface features. Measurements were performed over a variety of surfaces including water, farmland, mountain and desert areas. The magnitude of scatter coefficient and variations in its magnitude with viewing angle differ greatly for water and mountainous surfaces. Over water the scatter coefficient is high at normal incidence of the impinging electro-magnetic waves and falls off rapidly as the viewing angle departs from ninety degrees. Over mountainous areas the magnitude of scattering coefficient remains relatively constant over a 30-degree variation in viewing from 90 degrees and its value is of the order of 20 dB less than the maximum over-water value. Additional comparisons are made in the report of measurements made over farmland and desert areas. Included in the report is a detailed description of the measuring instrument.

This report is an expanded version of an earlier report issued by our group on the same subject and entitled "Flight Tests of a Radar Scattering-Coefficient Measuring Instrument."

ACKNOWLEDGEMENT

The work described in this report has been supported by the Lunar and Planetary Programs Branch of the Office of Space and Applications, NASA. The transmitter tube used in our equipment was developed under a program sponsored by the E/M Microwave Radiation Laboratory at the Electronics Research Center, NASA. We also wish to express our appreciation to the personnel at the NASA Ames Research Center who provided facilities for flight testing.

CONTENTS

LIST OF FIGURES

LIST OF FIGURES (Contd.)

I. INTRODUCTION

The research being conducted under the Venus Spacecraft Radar Program is directed toward on-board spacecraft experiments which will lead to a better understanding of planetary surfaces through microwave measurements.

This report describes an experiment using a radar-type instrument to measure the backscattering characteristics of Earth surfaces from an aircraft. The report is an expanded version of an earlier summary report previously issued.[1*] A pulsed-type X-band radar is used to measure the energy backscattered from an Earth-surface area at various angles of incidence, and this information allows gross features of the surface to be inferred. A number of experiments to measure the radar backscattering properties of the Moon and Venus have been performed from Earth-based radars.[2,3] These Earth-based radar measurements have been interpreted to estimate such properties as physical roughness and dielectric constant of a surface. The radar measurements to be described would give the same kind of information about surface properties as Earth-based microwave measurements but with the capability of higher resolution.

---

* Superscripts refer to numbered items in the Bibliography.

II. DEFINITION OF SCATTERING COEFFICIENT

The quantity measured by the radar instrument is the scattering coefficient. This quantity is defined as the ratio of power backscattered by the target to that which would be backscattered by a perfectly reflecting, hemispherical isotropic scatterer.[4] In terms of radar parameters, scattering coefficient is,

$$\Gamma(\theta) = \frac{2\pi R^2 W_r}{A_e W_t} \tag{1}$$

- $\Gamma(\theta)$ is the average scattering coefficient over the surface patch illuminated by the antenna beam.
- θ is the angle between the horizontal plane tangent to the surface patch and the antenna boresight axis ($\theta = 90^o$ represents normal incidence).
- R is the slant range between the radar and the surface.
- W_t is the energy in the transmitted pulse.
- W_r is the energy in the echo pulse.
- A_e is the effective receiving area of the antenna.

The concept of a scattering coefficient as a measure of surface characteristics applies primarily to surfaces which act as diffuse scatterers over the antenna beamwidth. For nondiffuse scatterers, that is, specular surfaces or those with only a few isolated strong scatterers within the beamwidth, the scattering coefficient is also useful.

Measurements of $\Gamma(\theta)$ can be made for a range of incidence angles by taking a separate data run at a number of discrete viewing angles, as depicted in Fig. 1a. In practice it is difficult to make data runs at various angles of incidence over exactly the same surface strip. Since most surfaces are reasonably homogeneous over some distance, however, it is possible to compare the results taken from separate runs over the same general area. In addition, the effect of the finite antenna beamwidth is to smooth local variations.

A sketch which qualitatively represents the scattering coefficient of two hypothetical surfaces is shown in Fig. 1b. The shape of the

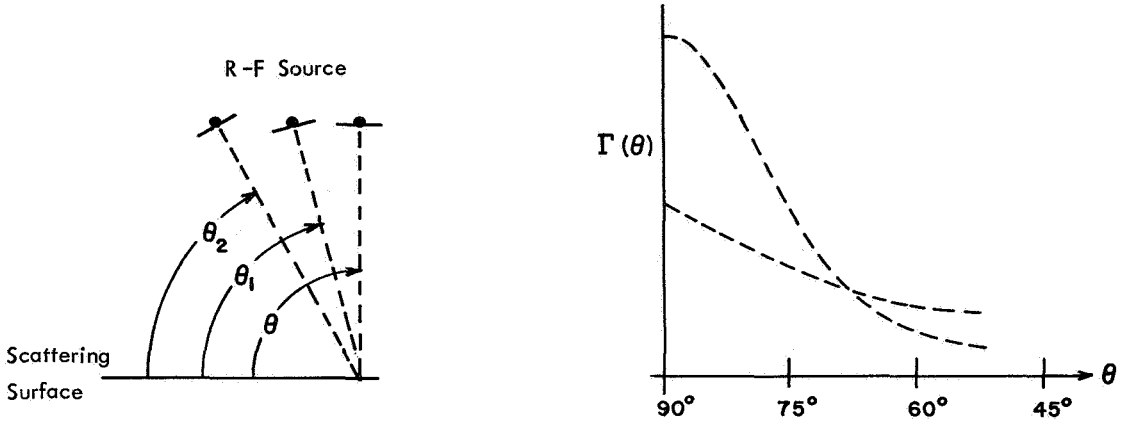

(a) Definition of Angle θ

(b) Representation of the Scattering Coefficients of Two Hypothetical Surfaces

Fig. 1 Geometry Associated with Measurements of $\Gamma(\theta)$

curves in Fig. 1b depends on the characteristics of the surface and also certain radar parameters. Since the objective is to ascertain surface characteristics from curves such as shown in Fig. 1b, it is necessary to know the effect of the radar parameters such as the frequency, beamwidth, and so forth. A practical way of determining these effects is to measure the scattering coefficient of surfaces whose gross characteristics are known and to use this data as a calibration for measurement of unknown surfaces.

III. FLIGHT-TEST SYSTEM PARAMETERS

An experiment was performed over selected target areas in the Western United States from a NASA CV-990 airplane. Some pertinent parameters of the radar employed in these measurements are listed below:

Frequency	9.72 GHz
Antenna	10" x 12" waveguide horn, linear polarization
Antenna Gain	25.6 dB
3 dB Beamwidths	8^{o} x 10^{o}
Transmitted Power	400 watts, peak

The transmitted waveform is shown in Fig. 2.

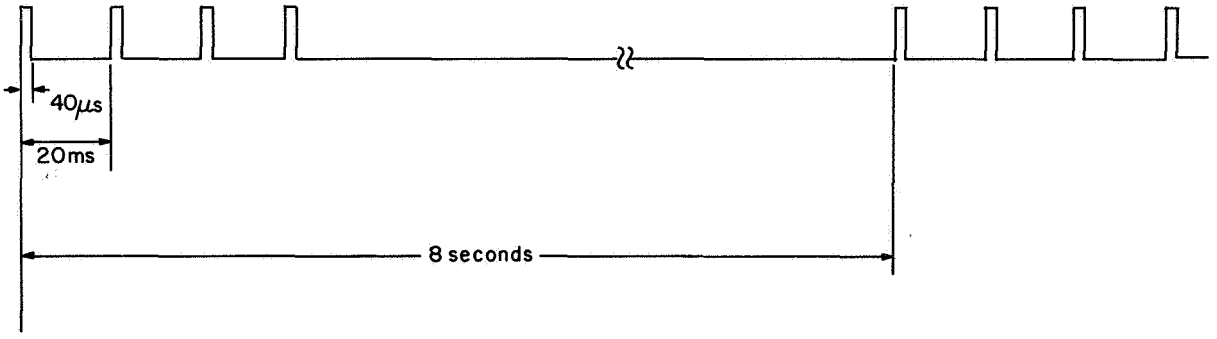

Fig. 2 Envelope of Transmitted Waveform

The aircraft flew at a nominal altitude of 35,000 feet so that the illuminated ground area corresponding to the 3-dB antenna beamwidth was a nearly circular patch roughly one mile in diameter. Only a single linearly polarized signal was transmitted and received. The

radar equipment was mounted in upright racks in the main compartment of the aircraft and connected to the antenna with a section of waveguide. At the average ground speed of the aircraft, 450 mph or 15 feet in 20 milliseconds, three overlapping measurements were taken during each burst. During the eight-second interval between bursts, the plane traveled approximately one mile, thus the next three measurements were taken from a ground patch contiguous with the previous area. Measurements were made at three discrete angles of incidence, 90° (normal incidence), 75° and 60°. It was possible to obtain data for the 75° and 60° angles of incidence by flying the aircraft in a circular course at bank angles of 15° and 30° respectively. The maximum angle was limited to 60° since the aircraft could not be flown in steeper bank angles.

A camera was mounted in the aircraft adjacent to the antenna, and its pointing axis was aligned parallel to the antenna pointing axis. The camera was slaved to the radar, and camera triggering was arranged so that one photograph was taken for each set of four transmitter pulses. Synchronization was such that the camera was triggered between 50 and 100 milliseconds after occurrence of the leading edge of the transmitter pulse. The camera viewing angle was approximately three times the antenna beam angle. Figure 3 shows the radar installation in the main cabin, and Fig. 4 shows the horn antenna and camera installation.

Figure 5 is a simplified block diagram of the radar equipment. A more complete diagram and description of the radar system are contained in the Appendix.

Calculation of the scattering coefficient through use of Eq. 1 requires knowledge of the energy transmitted, energy received, range and antenna aperture area. The energy transmitted, energy received and range are measured for each pulse by the radar; the antenna aperture area is a constant which has been calculated in two ways: (1) from the measured gain of the antenna and (2) by integration of the area under the E- and H-plane antenna-pattern measurements.

The range is measured between the leading edge of the transmitted pulse and the time when the detected echo pulse exceeds a threshold

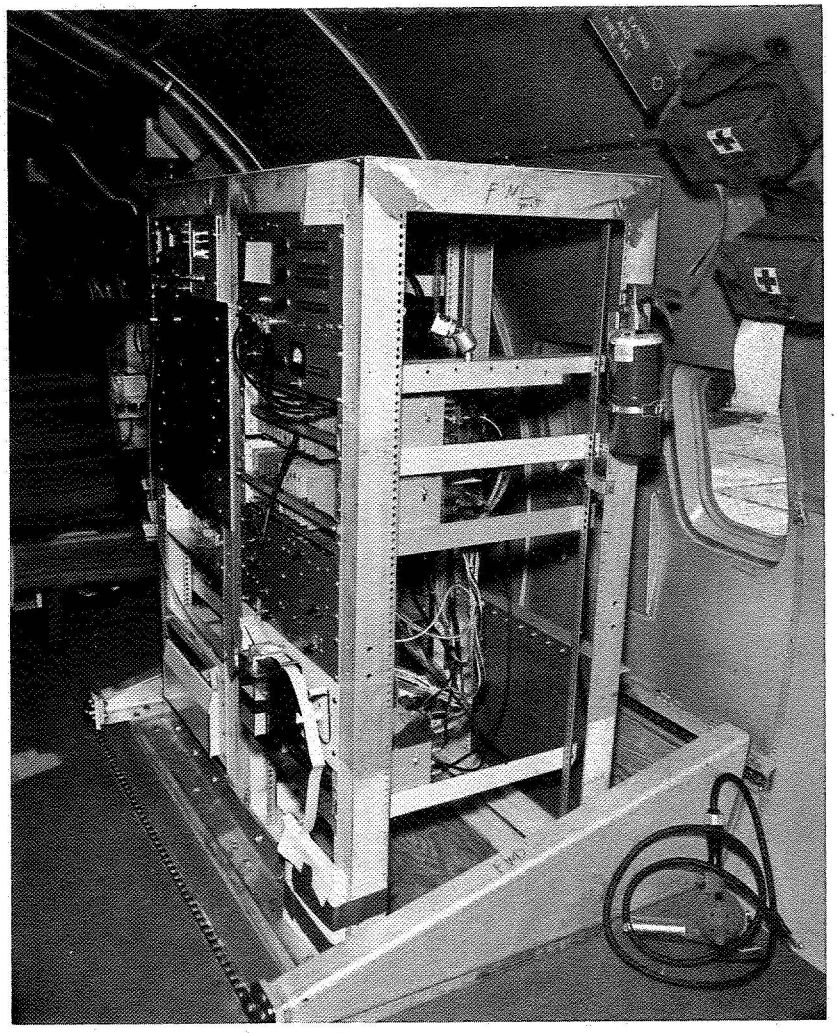

Fig. 3 Radar Installed in Cabin of CV-990

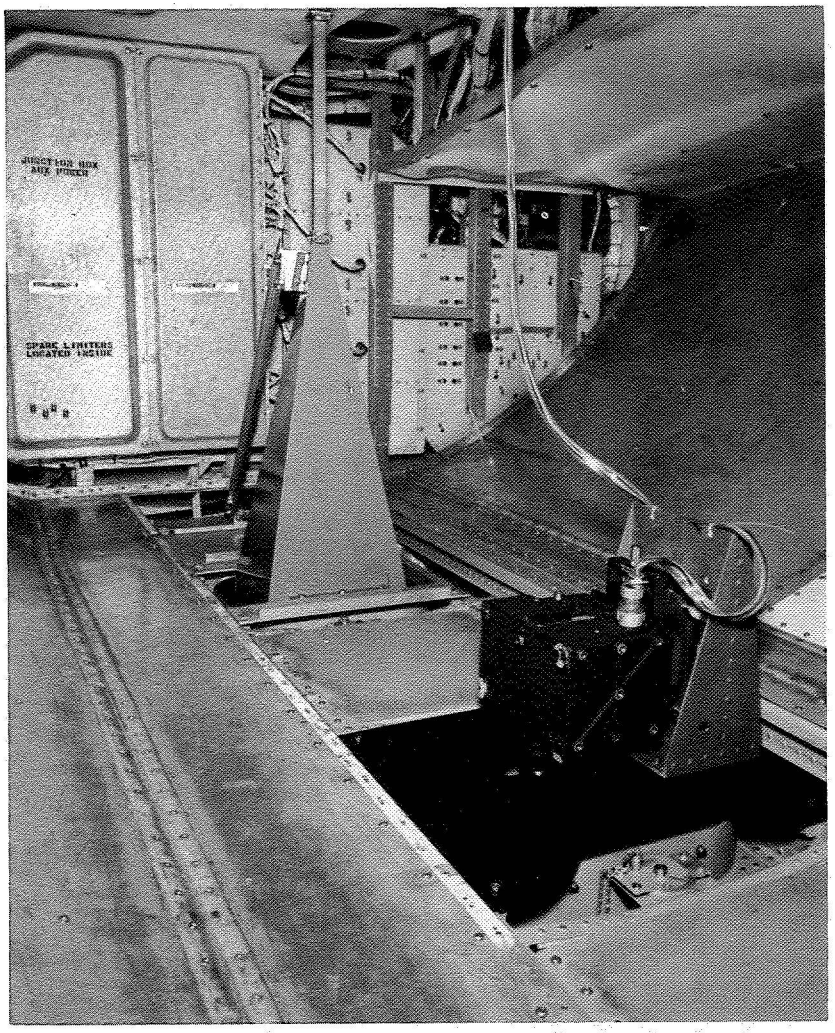

Fig. 4 Antenna and Camera Installed in CV-990 Cargo Area

level by counting the number of 1-MHz clock pulses in the time interval. The 1-MHz pulses counted in binary form are stored on paper tape.

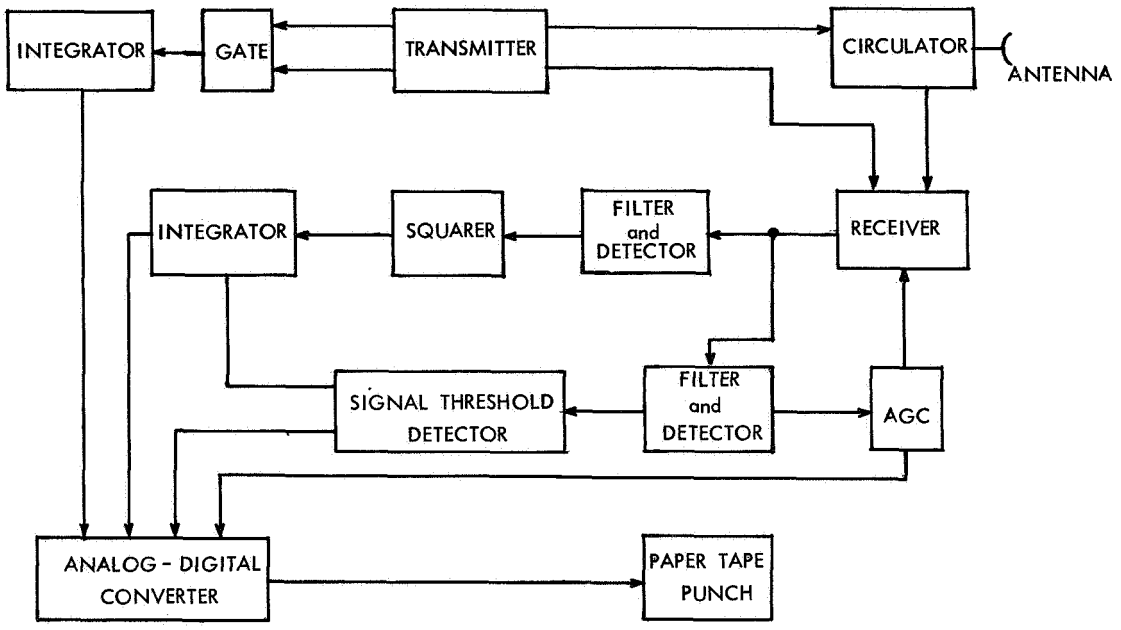

Fig. 5 Simplified Block Diagram of System

The energy transmitted is measured by detecting a sample of the klystron-transmitter power output by means of a diode detector. This diode detector is linear over a narrow range of power inputs so that its voltage output is proportional to power input. The detected voltage is integrated, converted to a binary number and stored on paper tape.

The energy-received measurement is performed on an amplified replica of the energy received at the antenna terminals. The signal received at the antenna terminals is translated in frequency to 30 MHz and amplified in a linear i-f amplifier. The gain of the i-f amplifier is controlled by an AGC circuit which can be adjusted in 3-dB steps over a 42-dB range. The voltage output of the i-f amplifier is envelope detected, squared, integrated, A-to-D converted and stored on paper tape. The gain of the i-f amplifier is adjusted so that the voltage output of the squarer does not saturate, and the AGC setting required is recorded on paper tape.

The accuracy of the radar system has been checked in the laboratory with a custom-designed simulator which gives measurements that can be repeated within 1 dB. In addition, continuous in-flight calibrations of the receiving channel insures that measurement accuracy is not degraded.

IV. PREFLIGHT-SYSTEM CALIBRATION

The scattering coefficient, as defined by Eq. 1, is

$$\Gamma(\theta) = \frac{2\pi R^2 W_r}{A_e W_t}$$

The received energy W_r' as measured at the output of the data processor is related to the actual energy received by the relation

$$W_r = k_r W_r' \tag{2}$$

where

W_r is the received energy

k_r is the receiver-channel calibration factor

W_r' is the received energy measured at the data processor output

In addition, the transmitted energy, as measured at the output of the data processor, is related to the actual transmitted energy as follows:

$$W_t = k_t W_t' \tag{3}$$

where

W_t is the transmitted energy

k_t is the transmitter-channel calibration factor

W_t' is the transmitted energy measured at the data processor output

The purpose of the comprehensive laboratory calibration procedure required for the instrument is to determine the conversion factors k_r and k_t. The measurement accuracy and degree of measurement repeatability is also accomplished during the calibration procedure.

The energy transmitted is measured by detecting a sample of the transmitted power with a point-contact diode detector and integrating

the detected voltage. A block diagram of the equipment used in calibrating a diode detector for power measurement is shown in Fig. 6.

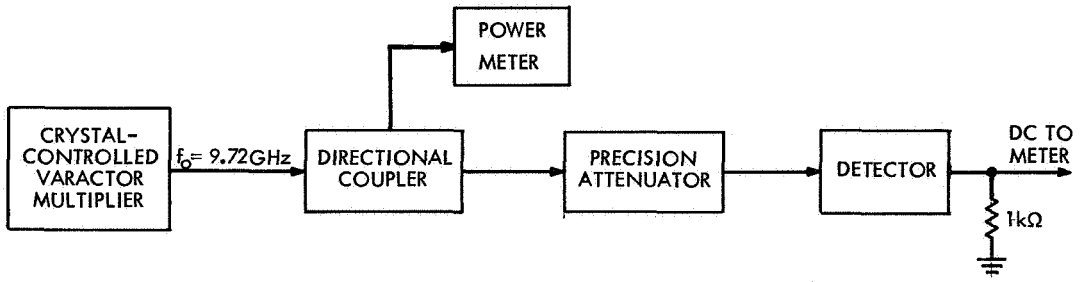

(a) BLOCK DIAGRAM OF EQUIPMENT FOR DIODE DETECTOR CALIBRATION

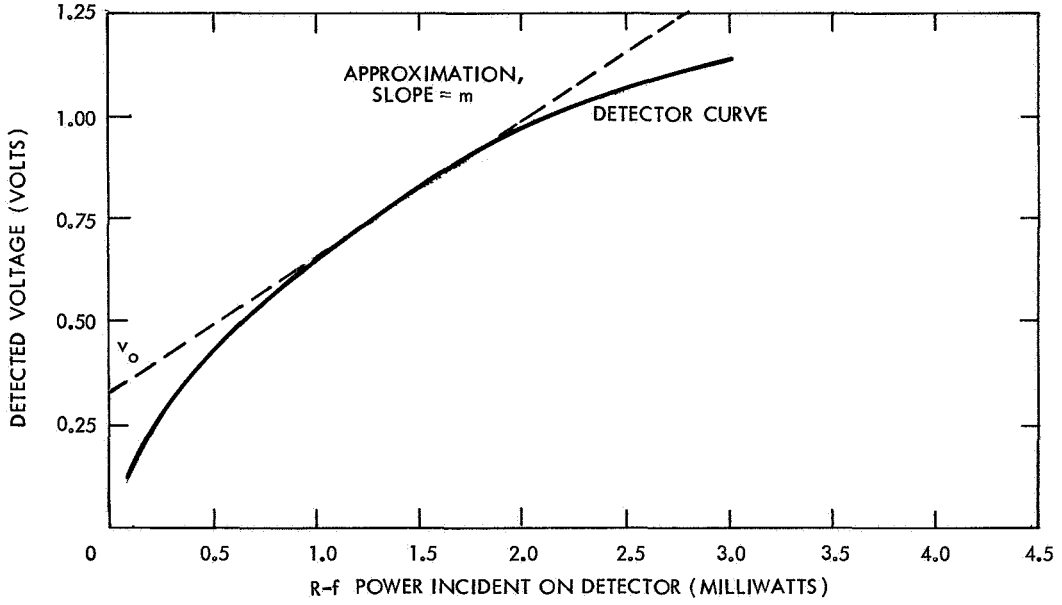

(b) CALIBRATION CURVE OF TYPICAL DIODE DETECTOR

Fig. 6 Diode Detector Calibration

The varactor-multiplier source generates c-w power which is measured by a power meter through a directional coupler. The power incident on the detector is varied by a precision attenuator with the detected voltage across a 1000-ohm load read on an accurate voltmeter.

The voltage-power curve of Fig. 6 represents calibration data taken from a typical diode detector. The dashed line drawn tangent to the curve defines a linear region of the curve which is used in the measurement. The equation for the line is

$$v = mp + v_o \qquad (4)$$

where

v is detected voltage

p is r-f power incident on detector

v_o is residual voltage at $p = 0$

Upon subtraction of v_o, the resultant voltage is proportional to power, which for pulse powers can be integrated to obtain the energy. The actual diode curve is linear over only a small region but this is acceptable for measuring any small variation in the transmitted energy which may exist.

The calibration procedure for the receiving channel involves the use of a simulator[5] to inject signals at the antenna input terminals. A block diagram of the simulator is shown in Fig. 7. The purpose of the simulator is to provide an accurately known signal at the power level expected at the antenna terminals. The simulated signal is generated by mixing a stable 9.69-GHz signal with a 30-MHz signal which can be either amplitude or frequency-modulated. The signal at 9.72 GHz at the output of the up-converter is selected by a narrow-band filter centered at 9.72 GHz and the level is measured with a calibrated diode detector. After passing through a directional coupler and a precision variable attenuator the signal is variable over a range from the minimum discernible signal to saturation of the receiving channel (from antenna input terminals to the binary output recorded on the paper tape). The receiving-channel gain is measured by injecting an unmodulated pulse of known power level and duration and recording the binary output representing the energy. This procedure is followed over the AGC range of the receiver and the data recorded is used to construct calibration curves, as shown in Fig. 8. The AGC numbers indicate the amount by which the i-f amplifier gain is decreased. For example, 0 dB means the i-f amplifier is at maximum gain. Thus, from knowledge of the AGC setting and measurements of the receiving-channel binary output, the energy present at the antenna terminals is determined.

To check the gain stability of the receiving channel during system operation an internal calibration signal of known energy is provided. A small portion of the r-f driver output at 9.72 GHz is routed by

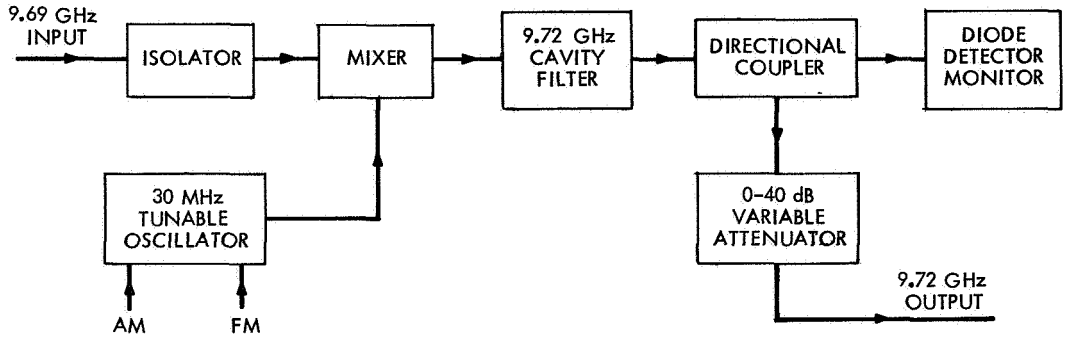

Fig. 7 Block Diagram of r-f Simulator

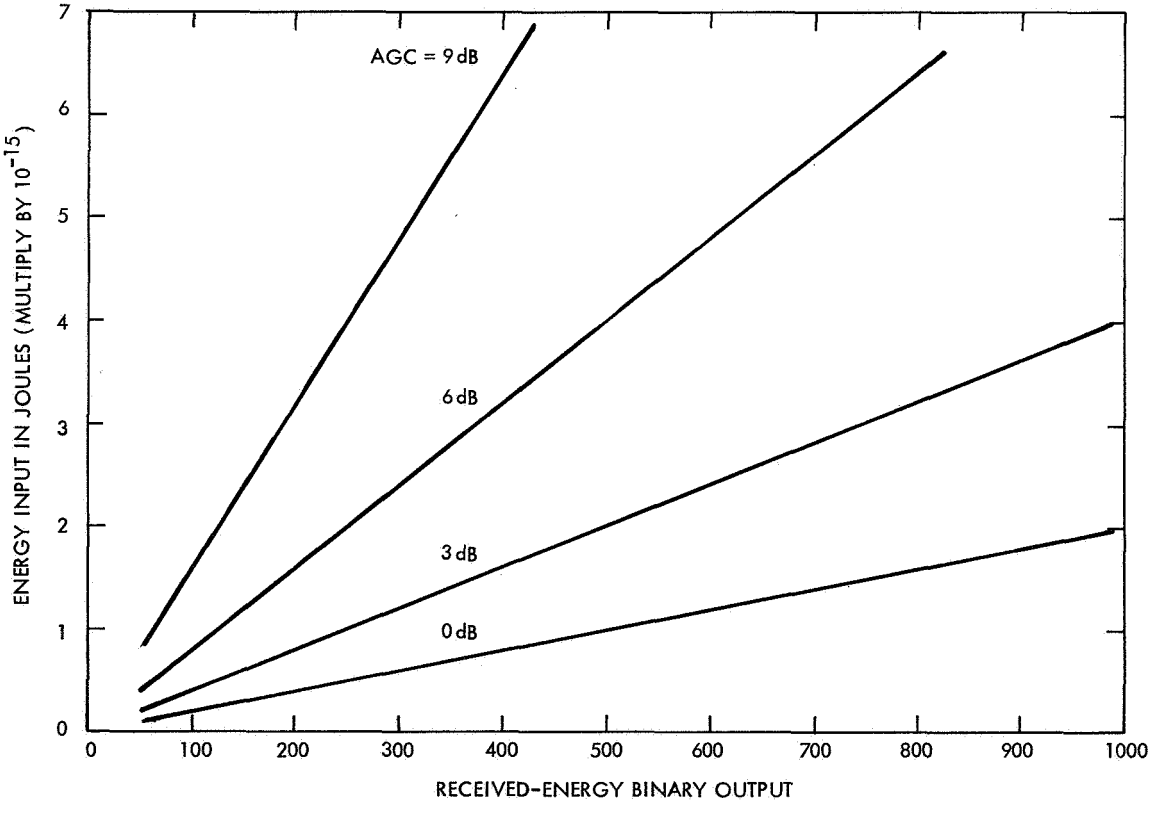

Fig. 8 Received Energy Calibration Curves

directional couplers to the mixer input, as shown in Fig. 20 in the Appendix. This internal calibration signal is timed to occur after the burst of received echo pulses. The AGC circuit is automatically set to a known AGC value during this time so that the calibration signal checks the receiving-channel gain at one point. This is noted in the system by monitoring the internal calibration energy binary output which remains constant if the receiving channel gain is constant. To insure that the internal calibration signal remains constant, the output of the r-f driver is monitored with a calibrated diode detector of the same type as used to measure the transmitter energy. The output of this detector is also integrated, A-to-D converted, and read in binary form.

The range measurement does not require calibration in the same sense as the energy measurements. The accuracy of the range measurement is checked by observing the time interval between the leading edge of the transmitted and simulated echo pulses on a calibrated oscilloscope.

The accuracy with which measurements can be performed is directly related to the accuracy and repeatability of the system-calibration factors described above. In general the calibration factors can be determined to a high degree of accuracy and repeatability for moderate or high signal-to-noise ratios. At low signal-to-noise ratios (as might occur in the measurement of received pulse energy) the noise causes the output to vary for constant inputs. In this case the calibration factor is determined by averaging over a number of output pulses. Another factor which affects repeatability of measurements is the possible sensitivity of circuits to temperature changes. Most of the circuits are designed to be temperature insensitive. The point-contact diodes used in the diode detectors are sensitive to extremes in temperature cycling and the characteristics are not exactly repeatable. The diode detectors used in this system have only been required to operate over a temperature change of less than 10^{o}C, and for this small change the diode characteristics are stable and repeatable.

The radar system is checked periodically to insure that the calibration factors are constant. For signal-to-noise ratios greater than 6 dB and constant temperatures the measurements are repeatable to

within ± 1 microsecond for range, ± 1/2 dB for energy transmitted and ± 1 dB for energy received. This results in scattering coefficient measurements being repeatable to within ± 1 1/2 dB.

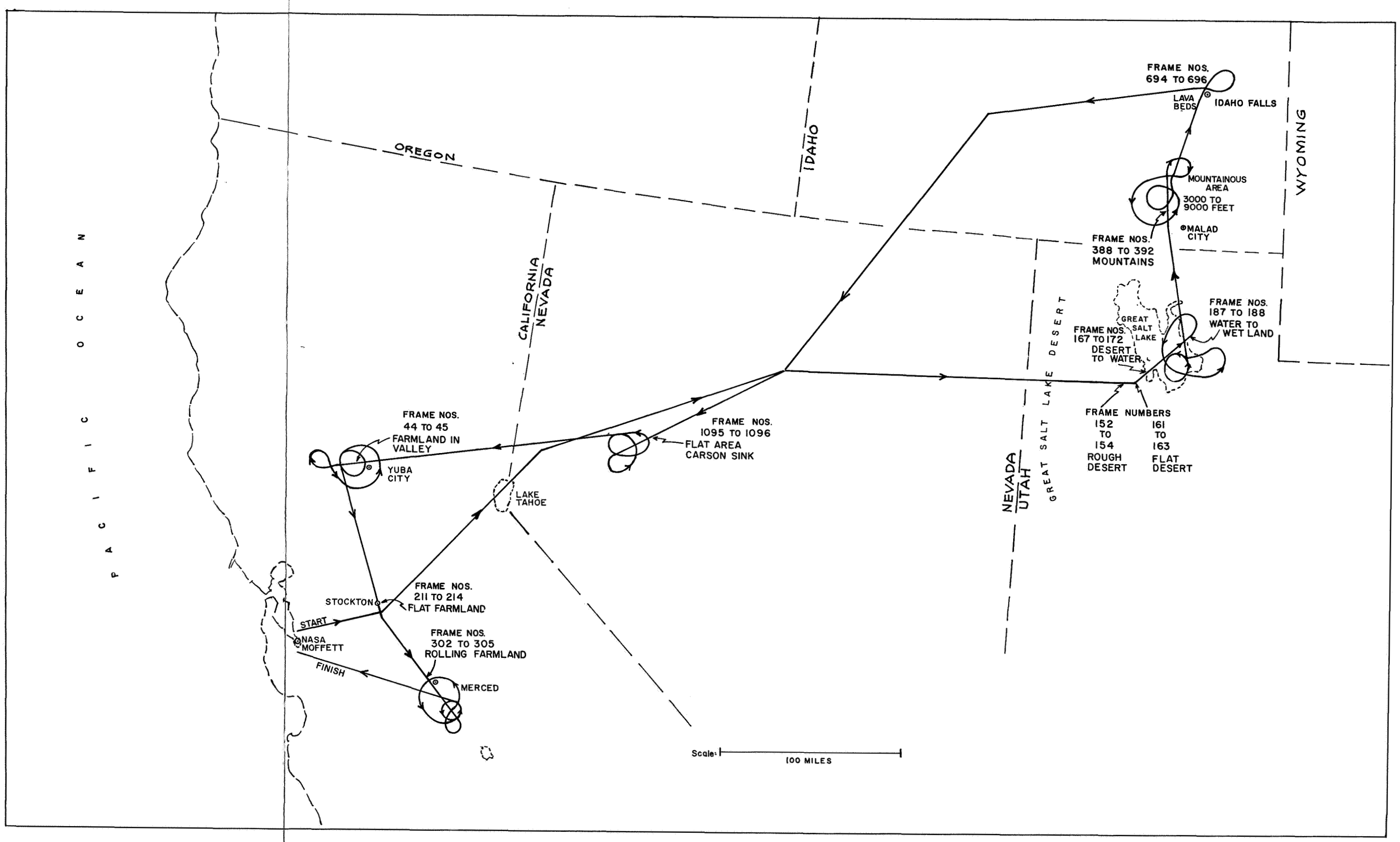

Fig. 9 Map of Flight Path for Measurement of Scattering Coefficients
October 11, 1967

V. FLIGHT-TEST RESULTS

The radar measurement system was flown in the CV-990 on October 10, 11 and 12, 1967. Several other experimenters from various organizations were on board the airborne laboratory during the same period. On October 10 and 12 the flight was under the guidance of the other experimenters. During these two days we were able to take data only when other experiments were not operating. On October 11 we specified the flight plan, which is shown in Fig. 9. Figure 10 is the flight track in the area of Los Angeles flown on October 12. We were able to take data over this flight track.

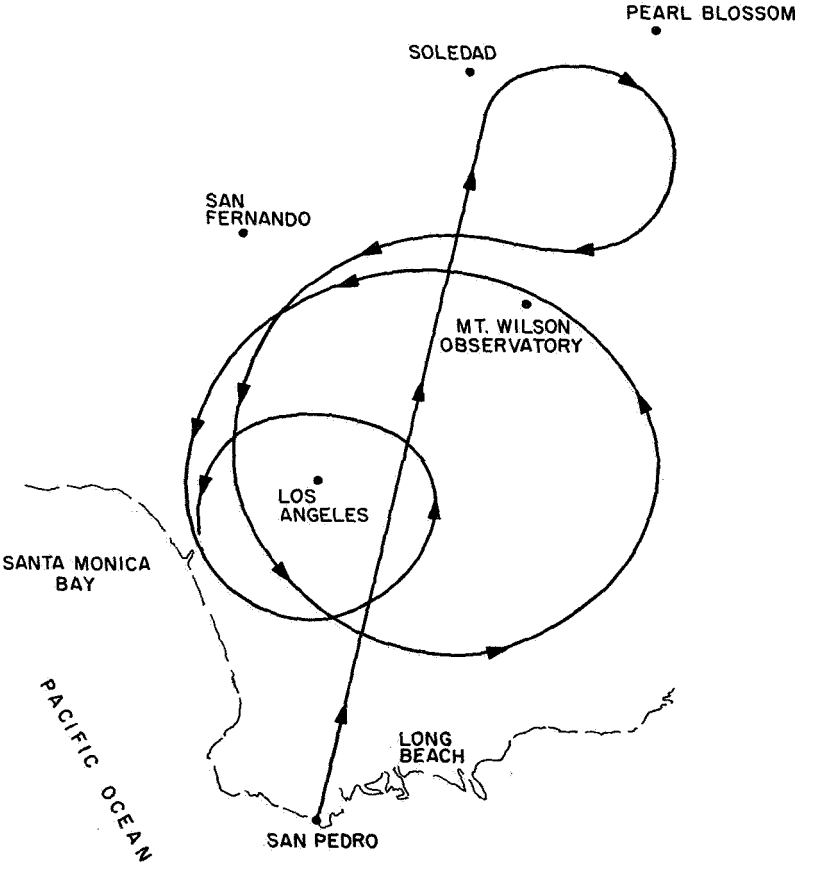

Fig. 10 Flight Track Over Los Angeles Area
October 12, 1967

The flight configuration which was necessary to make the required microwave measurements was determined by several factors. The basic requirement was that the aircraft fly over the same target area several times; first, on a straight level course; second, at a bank angle of 15 degrees; and third, at a bank angle of 30 degrees. The reason for this flight configuration was to obtain information on the same general area at oblique as well as normal incidence.

Another requirement was that the weather be clear during the measurement periods to allow the camera, located near the radar antenna, to photographically record the area being measured by the radar. Also, the type of target had to be easily distingiushable from an altitude of 35,000 feet. The antenna viewing area with the aircraft operating at this altitude was about one mile in diameter.

The areas of interest included smooth water, rougher water, both flat and rolling farmland, mountains and smooth terrain of the type found in certain desert areas.

The flight tests served two primary purposes. They furnished data on the backscatter properties of real surfaces and provided an engineering test of the radar-measuring system under field conditions. Observation of the radar system during the flight tests indicated that certain refinements to the system would be desirable for future flights. These system refinements are stated in Section VI. The data gathered during the flight tests are discussed in this section.

After the completion of the flight tests the data stored on paper tape along with appropriate calibration factors (as discussed in Section IV) were supplied to a digital computer. The computer furnished a numerical printout of the quantities measured and from these quantities calculated the scattering coefficient which was recorded on both cards and magnetic tape. The computer printout was carefully examined and it has been determined that approximately 40 percent of the data recorded is reliable and usable. The remaining data are unusable either because they fell outside the dynamic range of the receiving system or because of malfunctions in the data-recording system. In addition, the usable data have been compared with the film record to insure that the flight path over a target area did not include terrain which was not representative of the target area. For example,

if a small body of water appeared in the flight path over a target area which was predominantly farmland, the data from the water were not used.

The data remaining after these editing procedures are presented in graphical form in the set of figures that appear immediately after the Bibliography, Section VII. Figure 11 shows the mean value of the scattering coefficient at the three angles at incidence of 90°, 75°, and 60° for each of the seven target areas. The data used to compute the mean values of scattering coefficient are plotted in chronological form in Figs. 12a through 19a and in the form of histograms in Figs. 12b through 19b. Data were taken at only 90° incidence from lava beds in Idaho and only single plots have been included for this area. Also, insufficient data were collected over Salt Lake to furnish a meaningful plot at 60°.

The figures portraying the values of Γ in Figs. 12a through 19a require explanation. The burst numbers shown on the horizontal scale refer to the data recorded during a specific four-pulse burst. A unit change in burst number (e.g., 796 to 797) represents a change in time of approximately eight seconds. The vertical scale is the scattering coefficient, each point representing one of the three pulses in the burst. When there are fewer than three points for a burst number it indicates that the data was unusable for one of the reasons stated previously. Listed on these graphs are the mean ($\overline{\Gamma}$) and the standard deviation (σ) of the scattering coefficient, calculated for each angle of incidence from the equations,

$$\overline{\Gamma} = \frac{\Sigma \Gamma}{n} \tag{5a}$$

and

$$\sigma = \sqrt{\frac{\Sigma |\overline{\Gamma} - \Gamma|^2}{n}} \tag{5b}$$

where n is the number of points.

The histograms show the same data as illustrated in Figs. 12a through 19a but in a different form. The horizontal scale is the scattering coefficient divided into an arbitrary number of steps and the vertical scale is the ratio of the number of measurements in the interval to the total number of measurements taken at the particular angle of incidence.

The curves plotted in Fig. 11 are a useful method of presenting the data since the scattering behavior of the different surfaces can be easily distinguished. Qualitatively, the shape of the curves is related to surface roughness, and the area under the curves (if data were over a full hemisphere) is indicative of surface composition. The value of the scattering coefficient at any angle of incidence depends on two factors: the surface composition, which determines the total amount of energy reflected from the surface in all directions, and surface roughness, which determines the relative amount of energy reflected into any direction. Performing measurements which would allow the effects of surface roughness and composition on the scattering coefficient to be separated present difficult experimental problems. Although the curves of Fig. 11 represent the mean value of backscattering measurements made with an antenna of 8^{o} beamwidth at only three different incidence angles, the curves are useful for making relative comparisons between the various target areas.

The seven target areas can be grouped roughly into three categories on the basis of the angular behavior of the scattering coefficient. Salt Lake, the Pacific Ocean and the desert area near Carson Sink are classed as quasi-specular scatterers; the mountains near Malad are diffuse scatters; and Los Angeles and the farmland near Yuba City and Merced are a combination of quasi-specular and diffuse. The two extremes of behavior are represented by Salt Lake and the mountains near Malad. The mean scattering coefficient from Salt Lake decreases 22 dB from normal incidence to 75^{o} and 13 dB further from 75^{o} to 60^{o}. The mean scattering coefficient at Malad actually increases 1 dB from normal incidence to 75^{o} and then decreases by 4 dB from 75^{o} to 60^{o}. It is easy to distinguish between relatively calm bodies of salt water and mountains by their angular scattering behavior. A more difficult comparison is that between scattering coefficients of the ocean and of the relatively flat desert area near Carson Sink. The scattering curves of Fig. 11 have approximately the same shape, that is, the scattering coefficient for the ocean decreases 10 dB in the first 15^{o} and 16 dB in the next 15^{o}. In comparison the desert area decreases 15 dB in the first 15^{o} and 9 dB in the next 15^{o}. The ocean was fairly rough with whitecaps visible on the day the measurements were

made. Even so, the values of scattering coefficient were higher for the ocean than for the Carson Sink area. Furthermore, since the curves for the ocean and Carson Sink drop off quite rapidly, the area under the curves from just 90^{o} to 60^{o} (instead of over a hemisphere) is useful for comparing the total energy reflected from the two surfaces. Graphically integrating the area under the two curves gives the result that the area under the ocean curve is roughly four times the area under the Carson Sink curve. Presumably, this result is obtained because the salt water is a partial conductor even at 3 cm and thus reflects more energy than a nonconducting desert area.

The mean scattering coefficient curves for farmland near Yuba City and the rolling hills and farmland near Merced are quite similar, the values almost coinciding at 90^{o} and 60^{o}. This is a plausible result since the two areas are similar in surface roughness and composition. The Los Angeles area appears to be a diffuse scatterer except at normal incidence. The strong signals received at normal incidence are probably from flat areas such as rooftops or freeway surfaces.

The curves of Figs. 12a through 19a and 12b through 19b are intended to illustrate the time variation and distribution of the scattering coefficient. The points in Figs. 12a through 19a show the pulse-to-pulse variation during the 20-millisecond interval between successive pulses in a pulse burst. Also shown on the figures are calculated values of the mean and standard deviation of the scattering coefficient as defined in Eqs. 5a and 5b. The plane moved approximately 15 feet during the 20-millisecond time interval between pulses. Since the return signal varied considerably from pulse to pulse by as much as 16 dB, the conclusion is reached that 15 feet is greater than the decorrelation distance. Presumably, if the pulses were spaced successively closer together, some point would be reached where the pulse-to-pulse variation would be quite small. Apparently the surface roughness would have an affect on the required pulse spacing, that is, a truly smooth surface would give the same return from pulse to pulse regardless of the spacing. There is a possibility that an indication of surface roughness would result from measurements of decorrelation time. The

experiment performed had a fixed pulse spacing so there was no data gathered on pulses spaced closer than 20 milliseconds.

The histograms present the amplitude distribution of the scattering coefficient in a convenient form. The shape of the histograms suggests a Rayleigh distribution, but the paucity of data for some of the target areas does not permit a firm conclusion to be reached. The absence of data in some of the histogram intervals is due to an insufficient number of measurements. Most of the histograms resemble Rayleigh distributions in that the greatest number of points occur in the first interval, and the mean and standard deviation are approximately equal. When the data are Rayleigh-distributed it indicates that the received signal is the sum of a large number of small signals of almost constant amplitude and random phase. Some of the histograms, however, do have the largest number of points in the second interval, for example, the histograms for the ocean at 75^{o} and 60^{o}. This indicates that the scattered signal is the sum of a constant signal plus a large number of small random signals.

VI. CONCLUSIONS

The flight-test experiment described in this report, which was performed to demonstrate the engineering feasibility of the measuring instrument and to gain insights into the character of backscattering data that could be obtained, was successful. A productive amount of data on the X-band backscattering properties from a variety of surfaces were recorded. Analysis of these data leads to the conclusion that gross surface features can be deduced by measurements of this kind. In particular, the mean scattering coefficient, when measured as a function of angle of incidence of the impinging radiation, has proved to be an effective method for interpreting the data.

The electromagnetic-radiation-measurement equipment used in the system, in general, performed satisfactorily. However, results indicate that certain performance improvements can be attained. Specifically, the following modifications should be made:

1. Redesign of the receiver automatic gain control system to accommodate the large pulse-to-pulse amplitude variations in the echo signals.

2. Increase the system duty factor to allow the gathering of more data in less flight time.

3. The capability to alter the transmitted waveform during flight to observe the effects of surface properties on the decorrelation time of the scattering coefficient.

Consideration has been given to methods of gathering additional information for the purpose of identifying surface features. One possibility is the use of a radar and radiometer operated as a dual-mode measurement instrument. The instrument, for which we have a tentative design, would operate in the radar mode to gather backscatter measurements. In the radiometer mode, radiant-temperature measurements would be made of the surface of interest. Radiometer measurements would be made during radar off-time and would utilize the radar-receiver circuitry. It is estimated that a dual-mode

measuring instrument would consume approximately 10 percent additional prime power and would be about 10 percent heavier than the present radar-measuring system.

VII. BIBLIOGRAPHY

1. Reintjes, J. F. et al., "Flight Tests of a Radar Scattering-Coefficient Measuring Instrument," M.I.T. Electronic Systems Laboratory, Report ESL-R-340, February, 1968.

2. Pettingill, G. H. et al., "A Radar Investigation of Venus," Astron. Journal, Vol. 67, 181, 1962.

3. Evans, J. V. et al., "Radio Echo Observations of Venus and Mercury at 23 cm Wavelength," Astron. Journal, Vol. 70, No. 7, pp. 486-501, September, 1965.

4. Davies, H., and Mac Farlane, G. G., "Radar Echoes from the Sea Surface at Centimeter Wavelengths," Proc. Phys. Soc., Vol. 58, Pt. 6, No. 330, pp. 717-729, November, 1946.

5. Arnn, E. L., "A Special-Purpose X-Band Radar-Target Simulator," Master of Science Thesis, Electrical Engineering Department, M. I. T., September, 1965.

6. M.I.T. ESL Report VA-909B Klystron - Final Report. To be published.

7. Bosco, J. A., and Roberge, J. K., "High Efficiency D-C to D-C Converter-Regulators," M.I.T. Electronic Systems Laboratory, Report ESL-R-288, November, 1966.

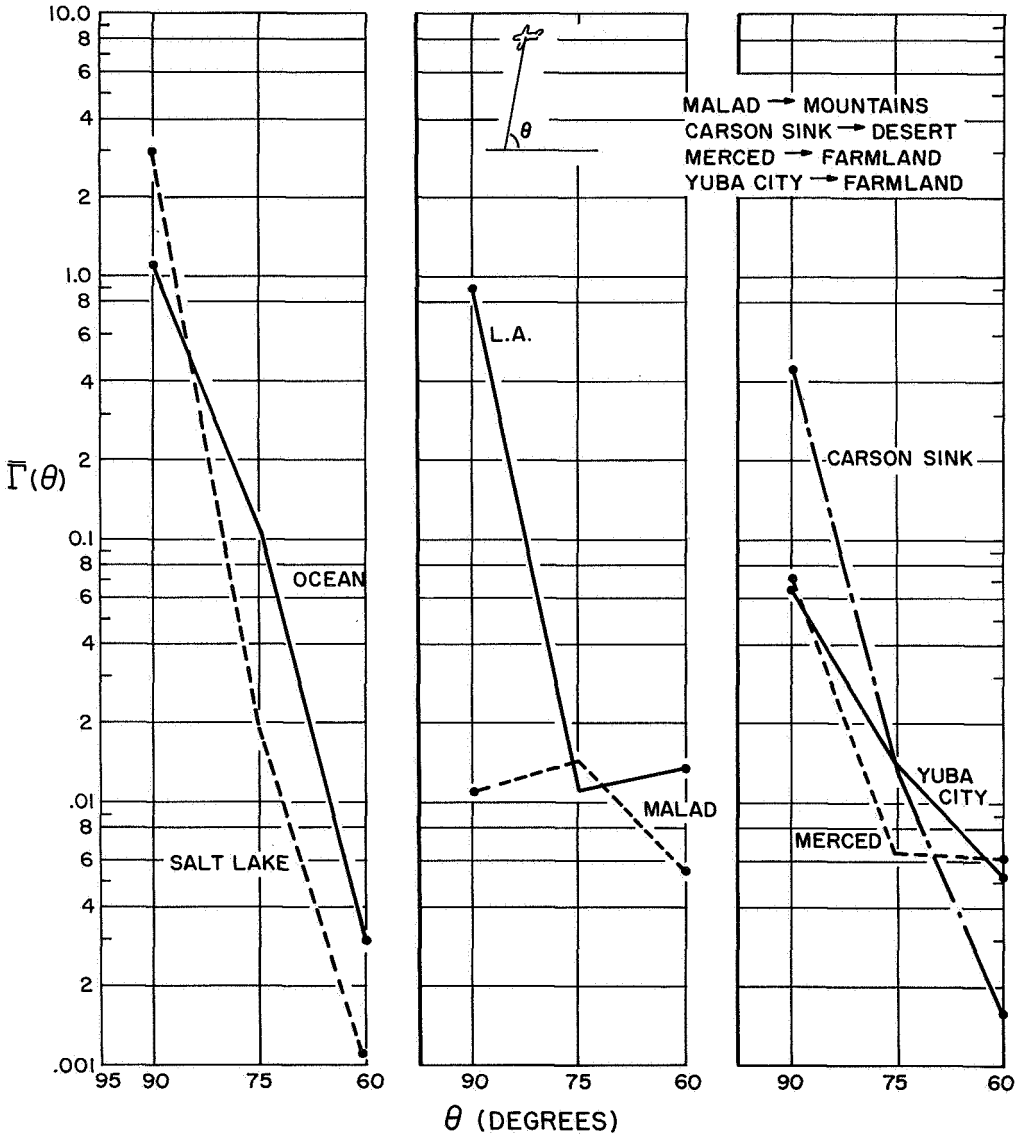

Fig. 11 Mean Value of Scattering Coefficient as a Function of the Angle of Incidence

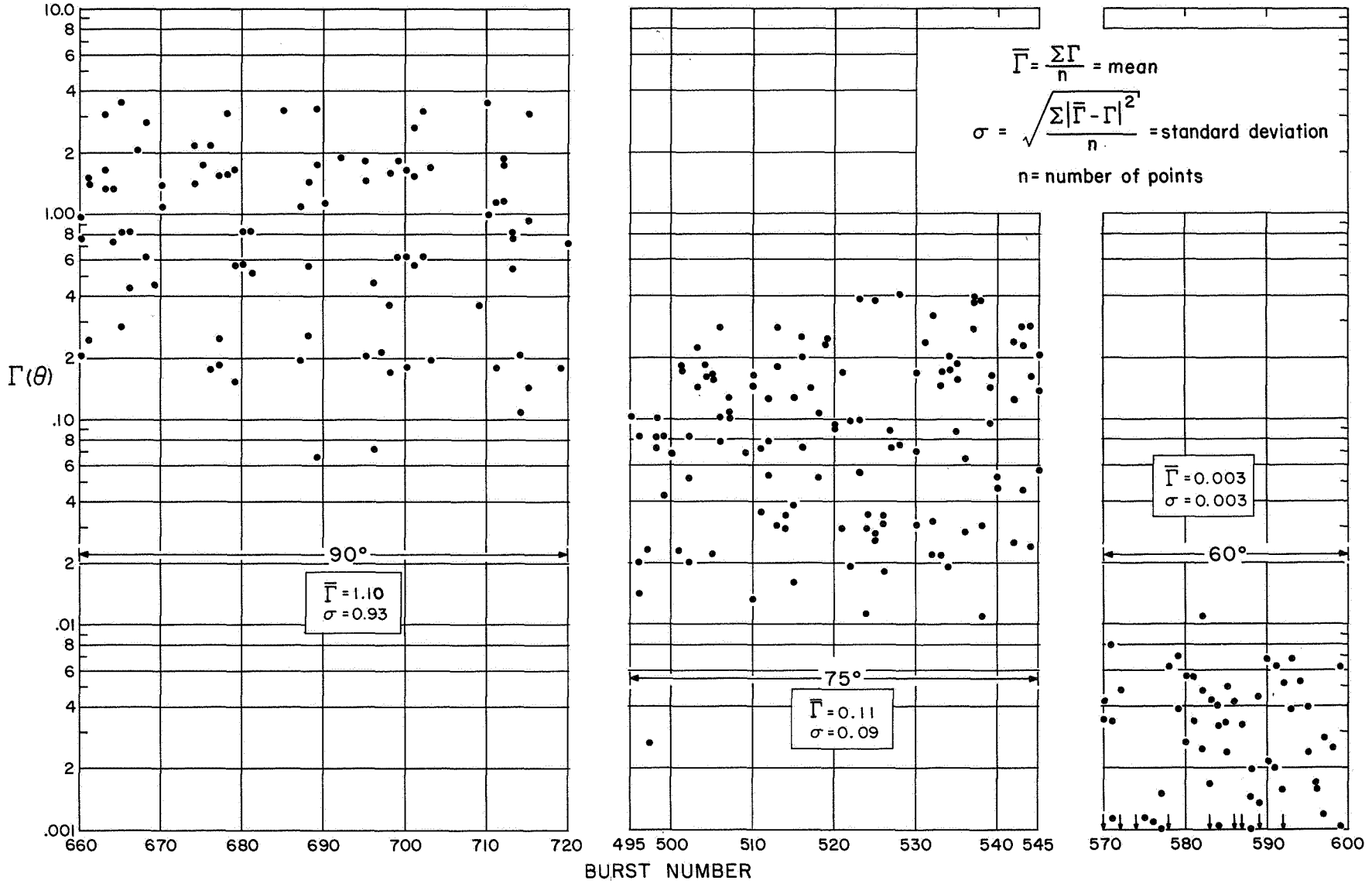

Fig. 12a Scattering Coefficient Measurements as a Function of Time
Pacific Ocean

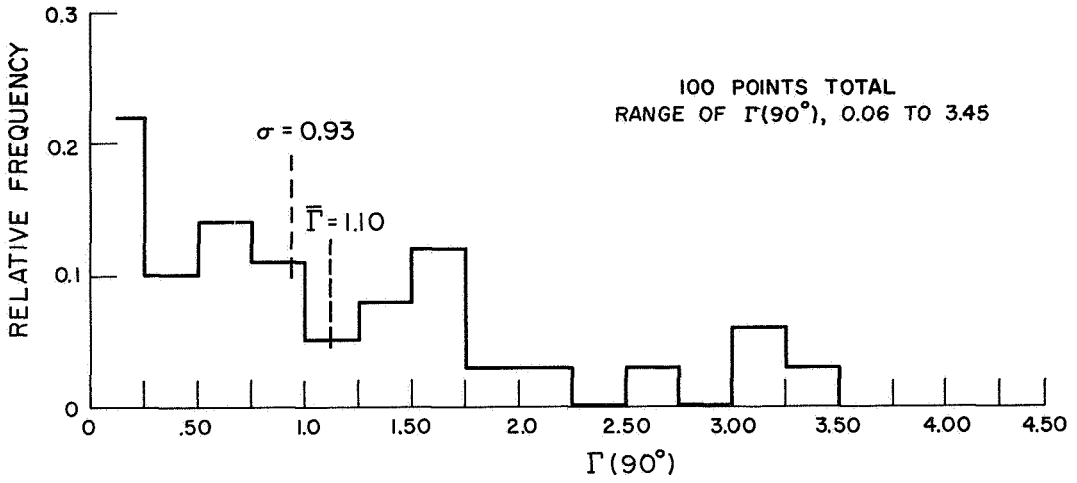

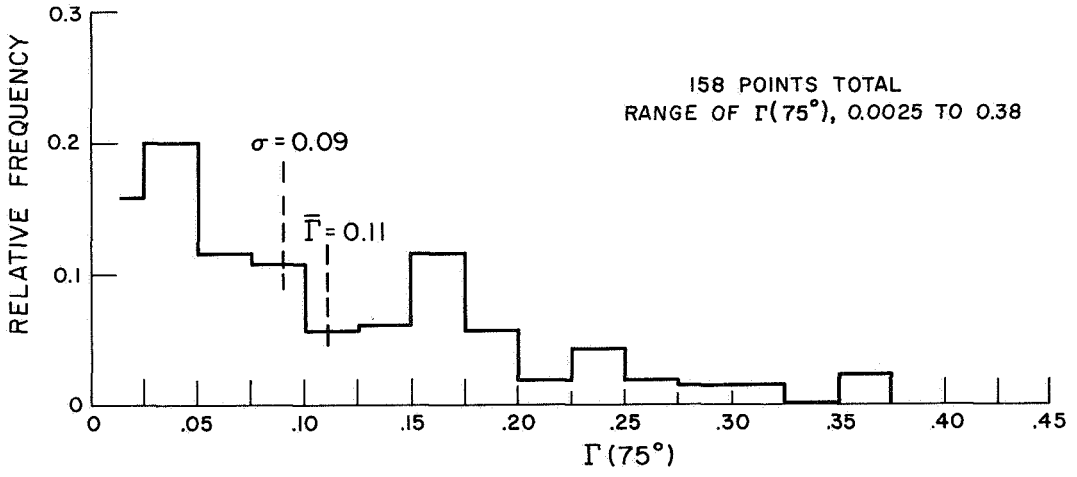

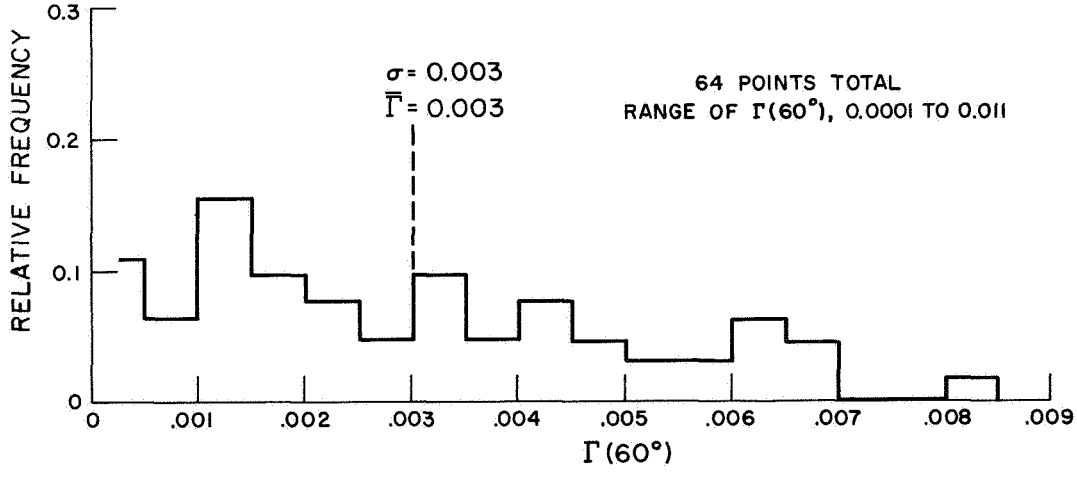

Fig. 12b Histograms of Scattering Coefficient Measurements
Pacific Ocean

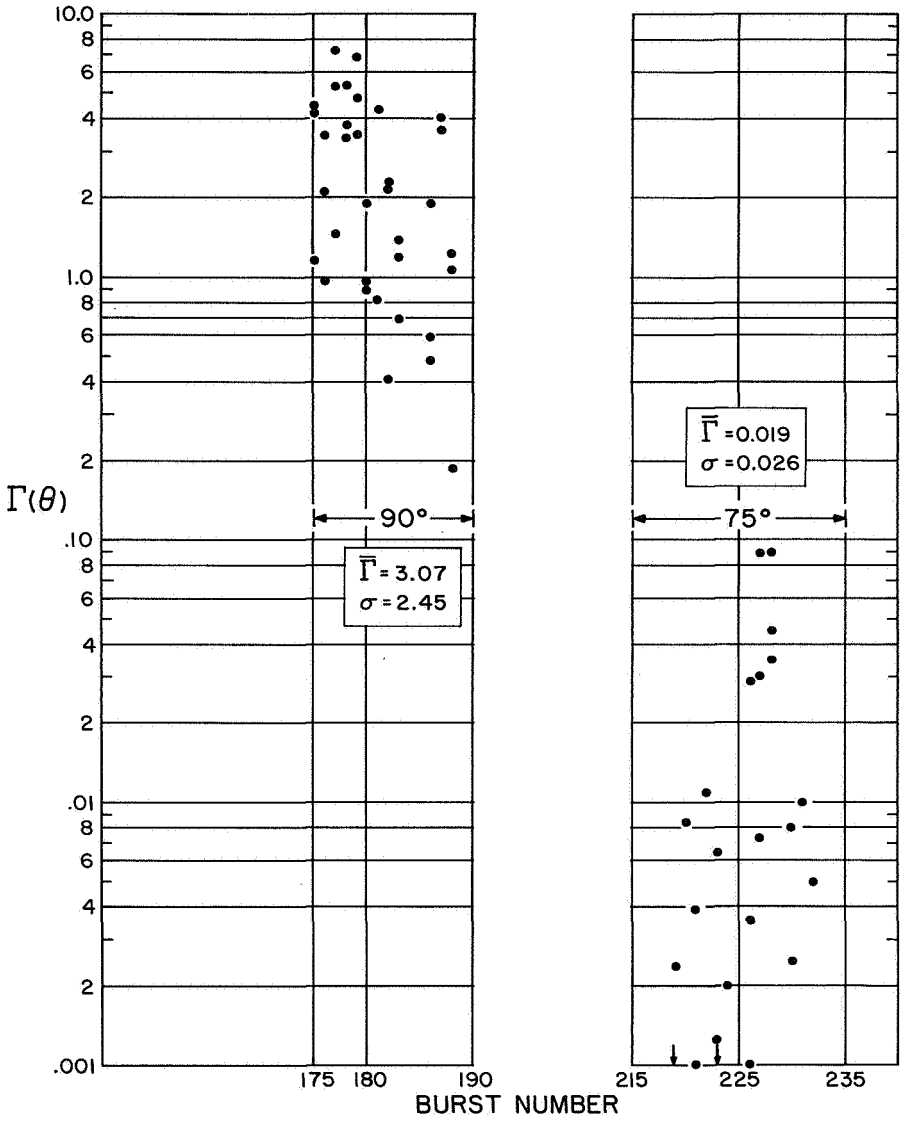

Fig. 13a Scattering Coefficient Measurements as a Function of Time
Great Salt Lake, Utah

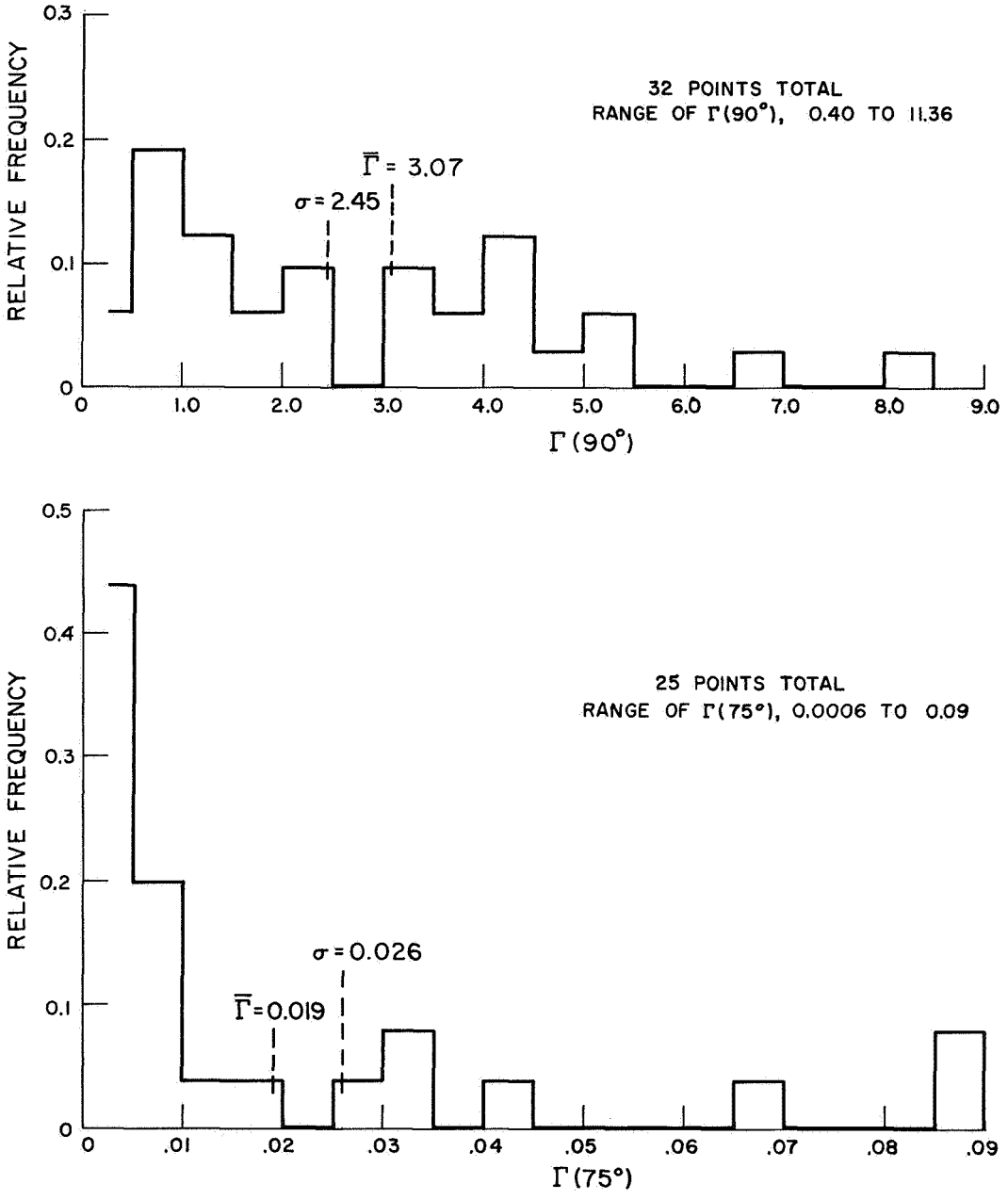

Fig. 13b Histograms of Scattering Coefficient Measurements
Great Salt Lake, Utah

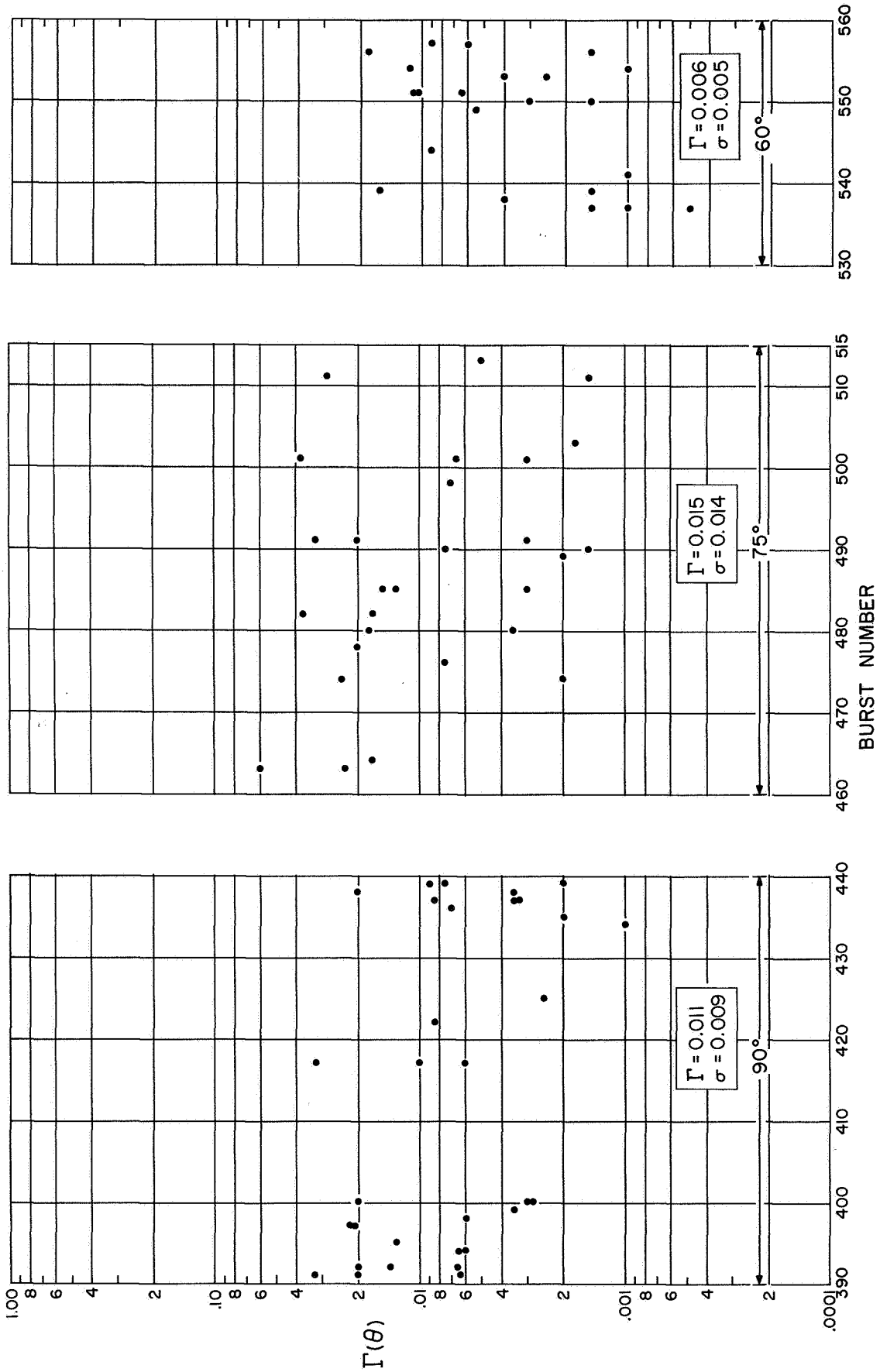

Fig. 14a Scattering Coefficient Measurements as a Function of Time
Malad, Idaho (Mountains)

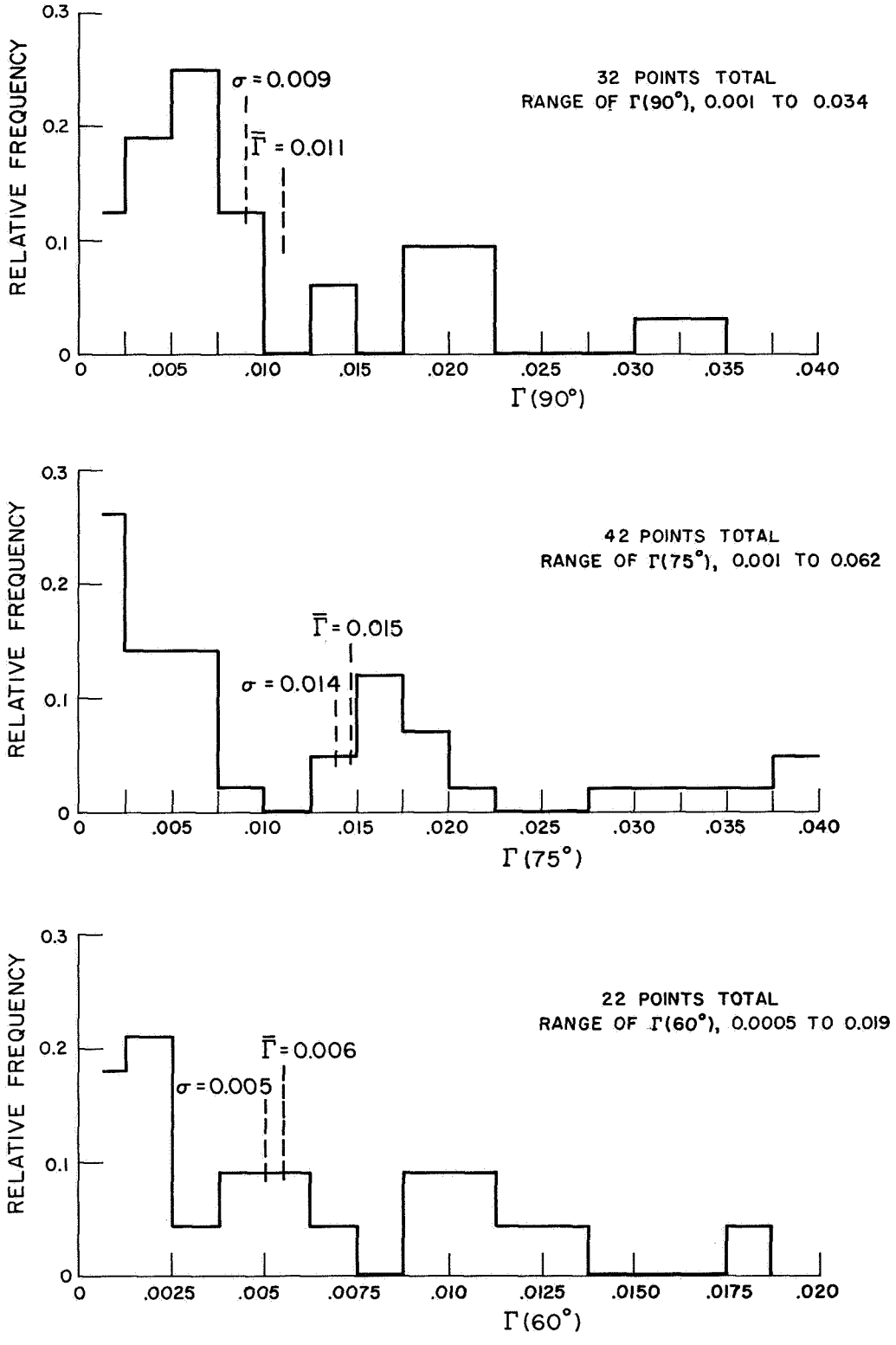

Fig. 14b Histograms of Scattering Coefficient Measurements
Malad, Idaho (Mountains)

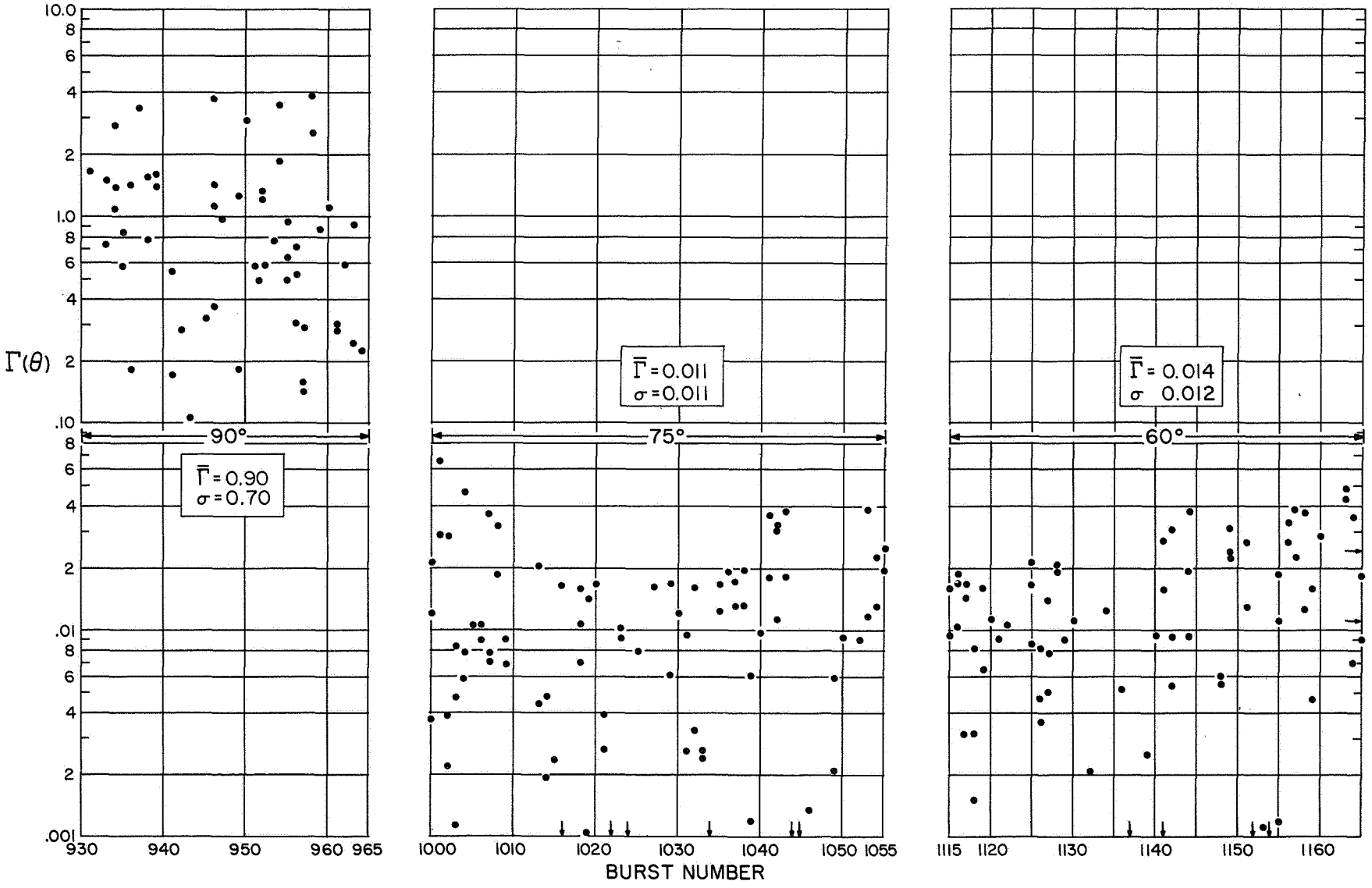

Fig. 15a Scattering Coefficient Measurements as a Function of Time
Los Angeles, California

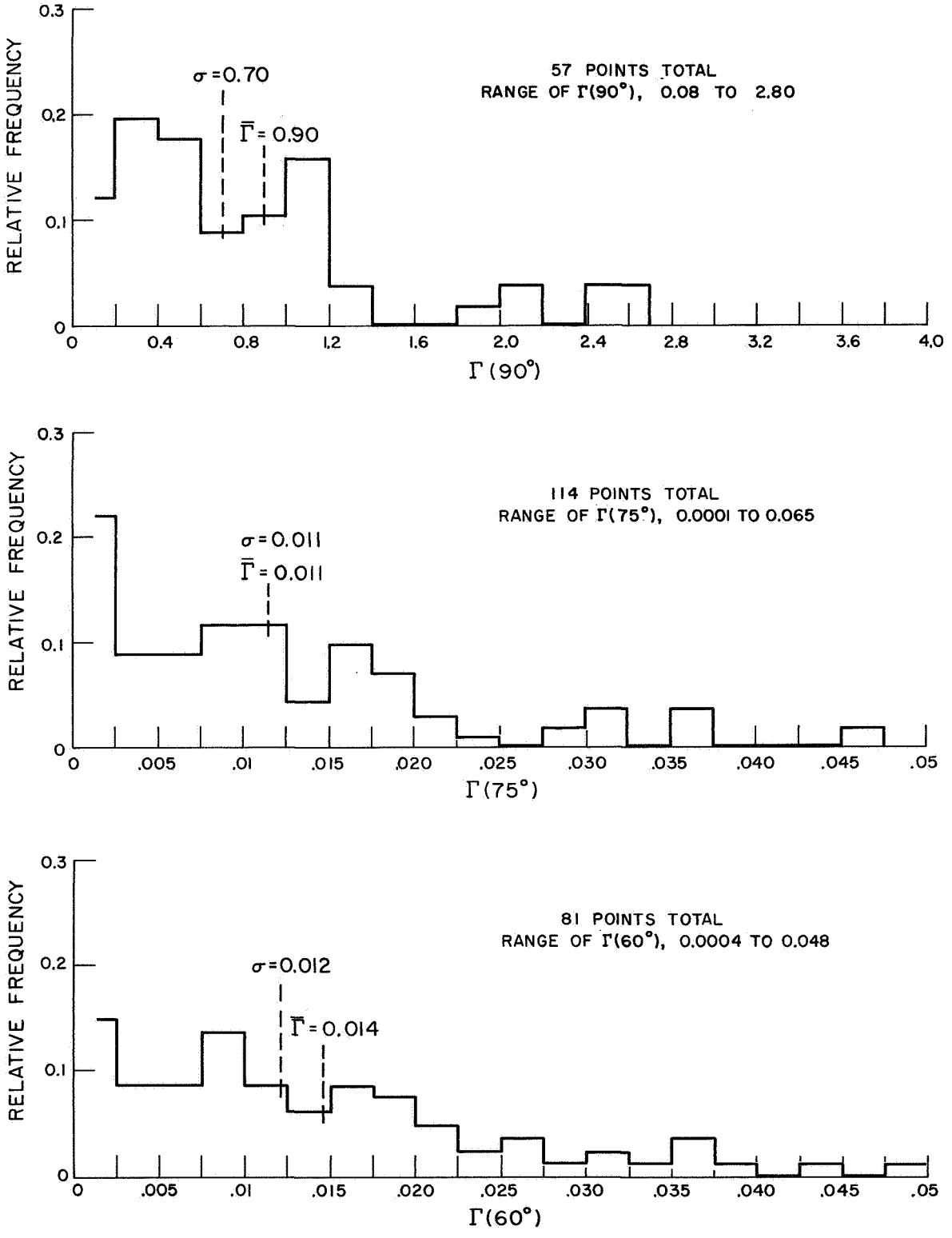

Fig. 15b Histograms of Scattering Coefficient Measurements
Los Angeles, California

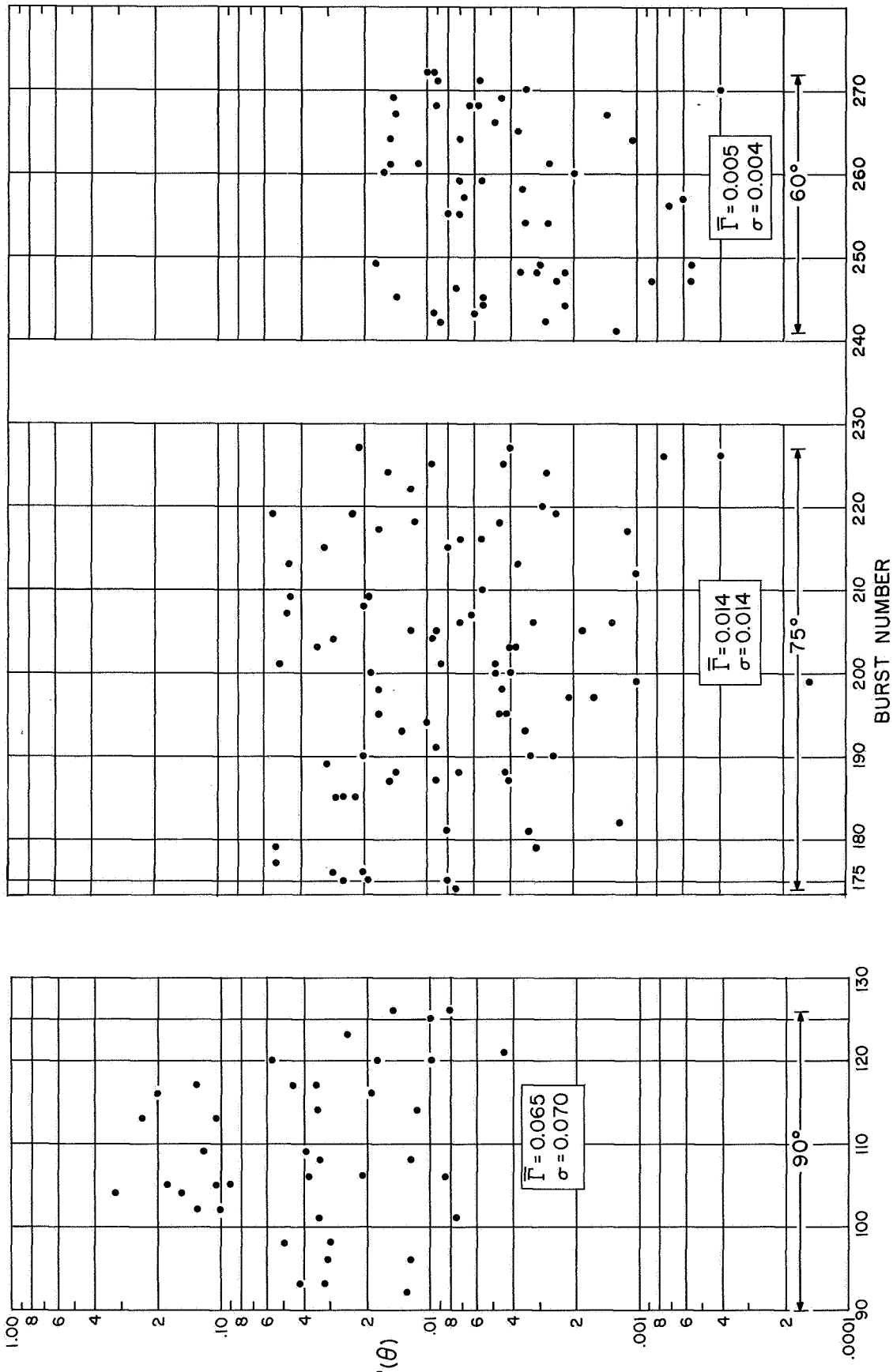

Fig. 16a Scattering Coefficient Measurements as a Function of Time
Yuba City, California (Farmland)

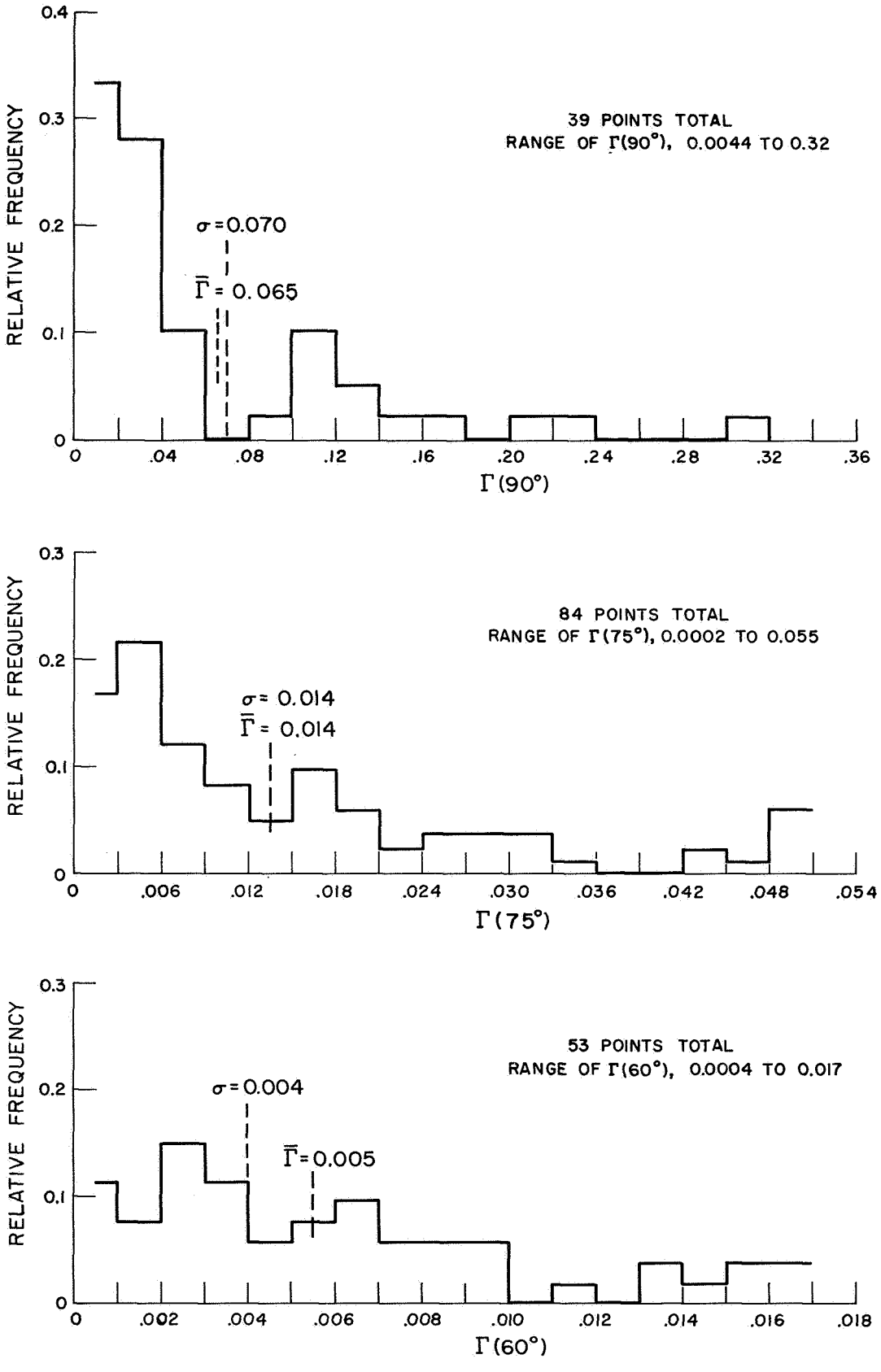

Fig. 16b Histograms of Scattering Coefficient Measurements
Yuba City, California (Farmland)

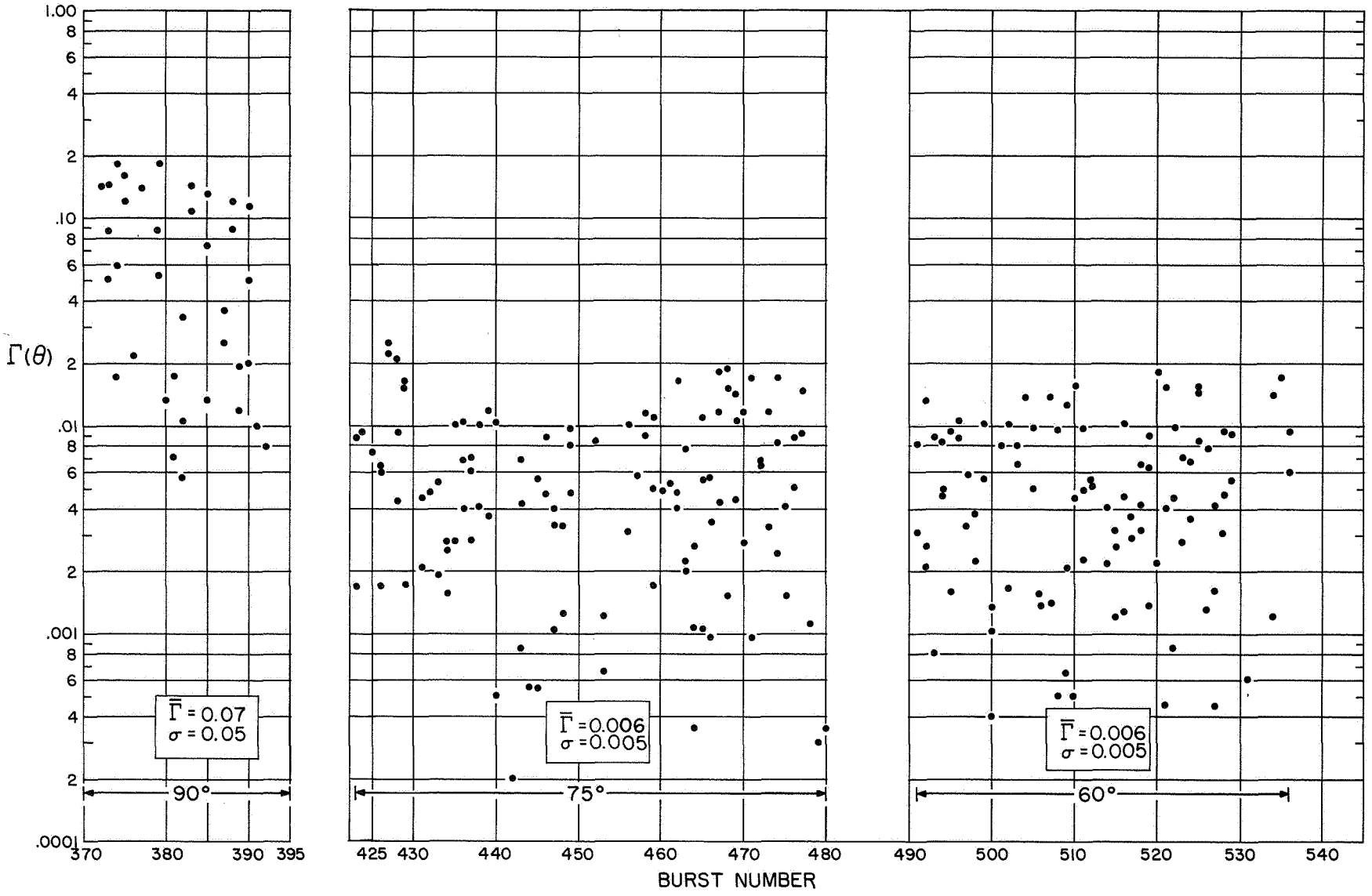

Fig. 17a Scattering Coefficient Measurements as a Function of Time
Merced, California (Rolling Farmland)

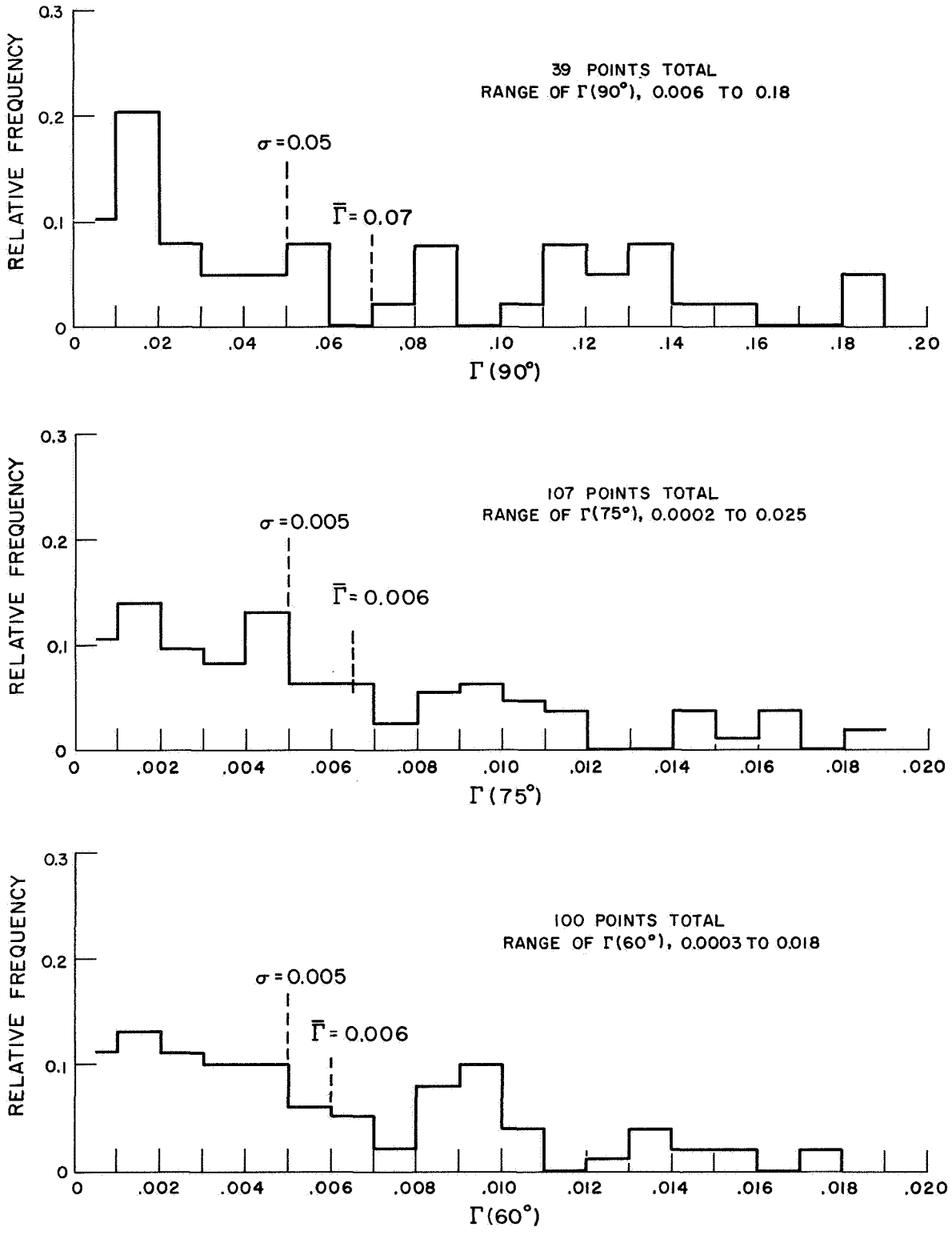

Fig. 17b Histograms of Scattering Coefficient Measurements
Merced, California (Rolling Farmland)

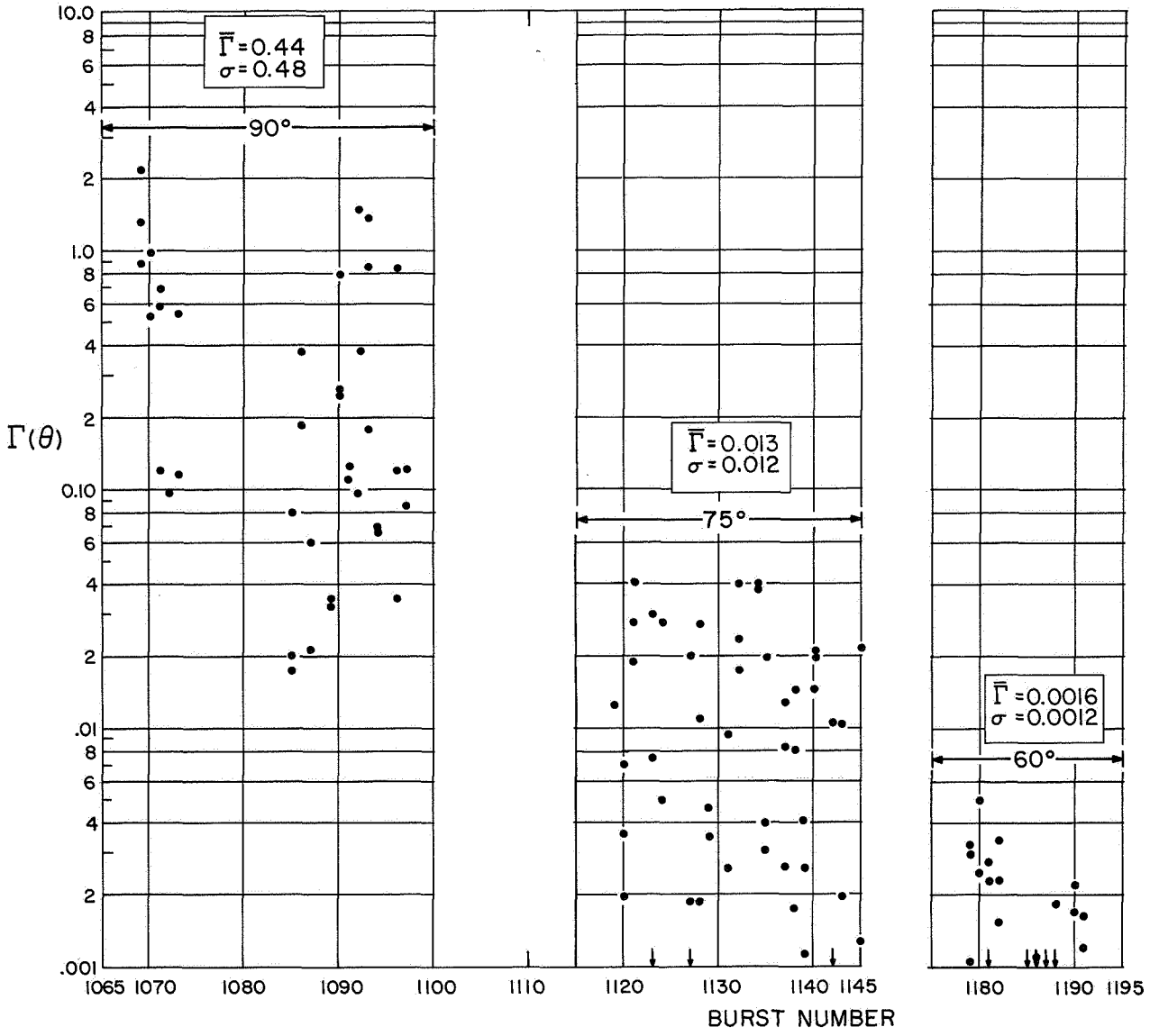

Fig. 18a Scattering Coefficient Measurements as a Function of Time
Carson Sink, Nevada (Desert Area)

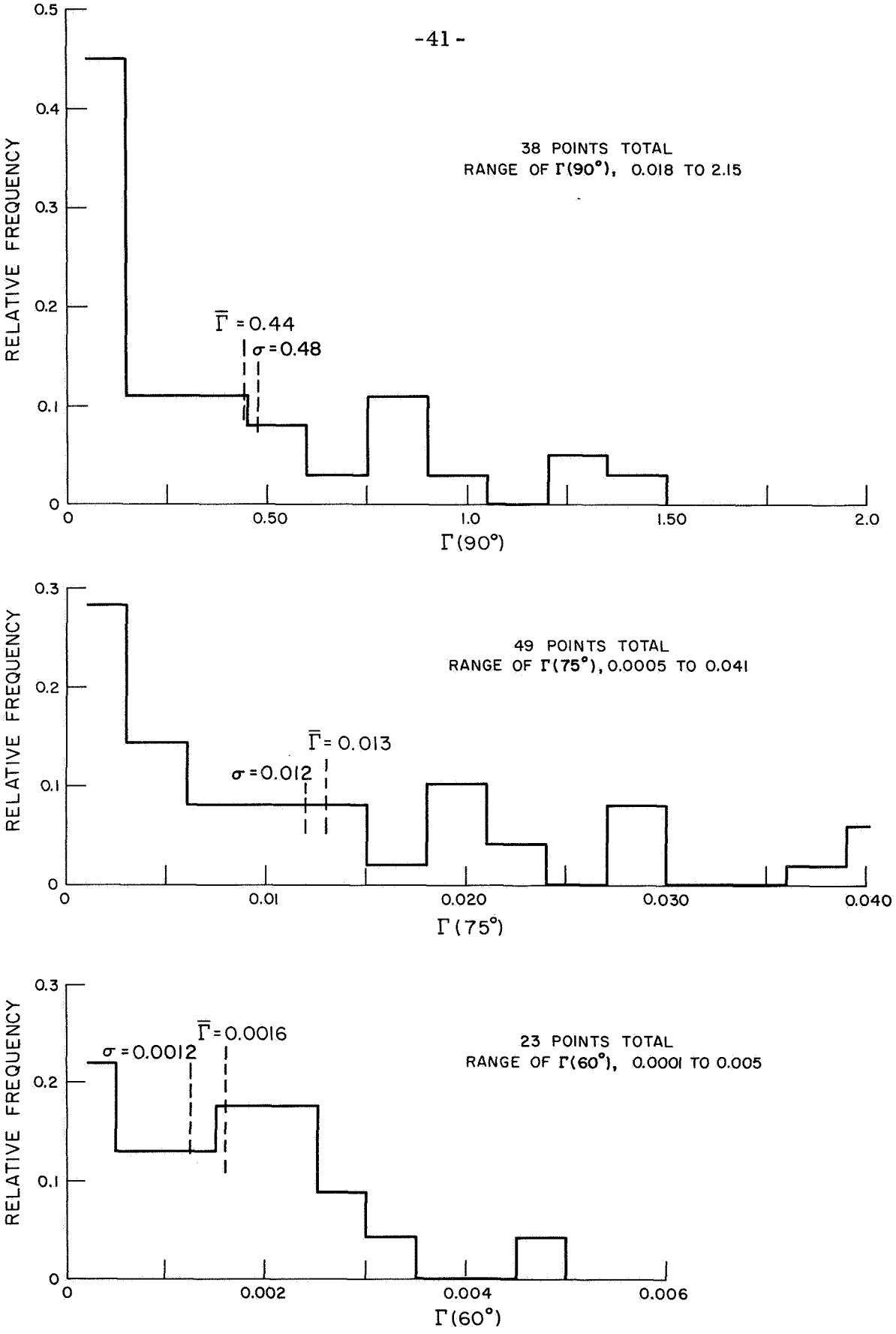

Fig. 18b Histograms of Scattering Coefficient Measurements
Carson Sink, Nevada (Desert Area)

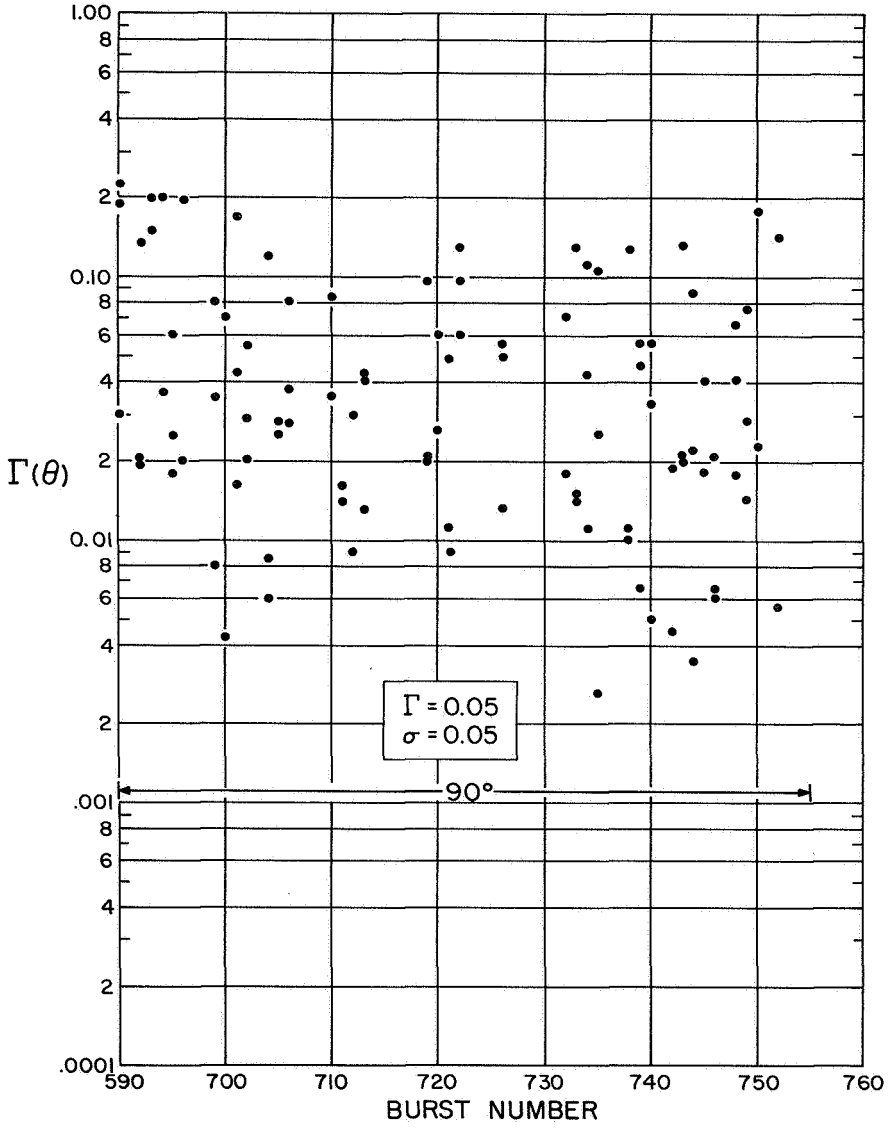

Fig. 19a Scattering Coefficient Measurements as a Function of Time
Idaho Falls, Idaho (Lava Beds)

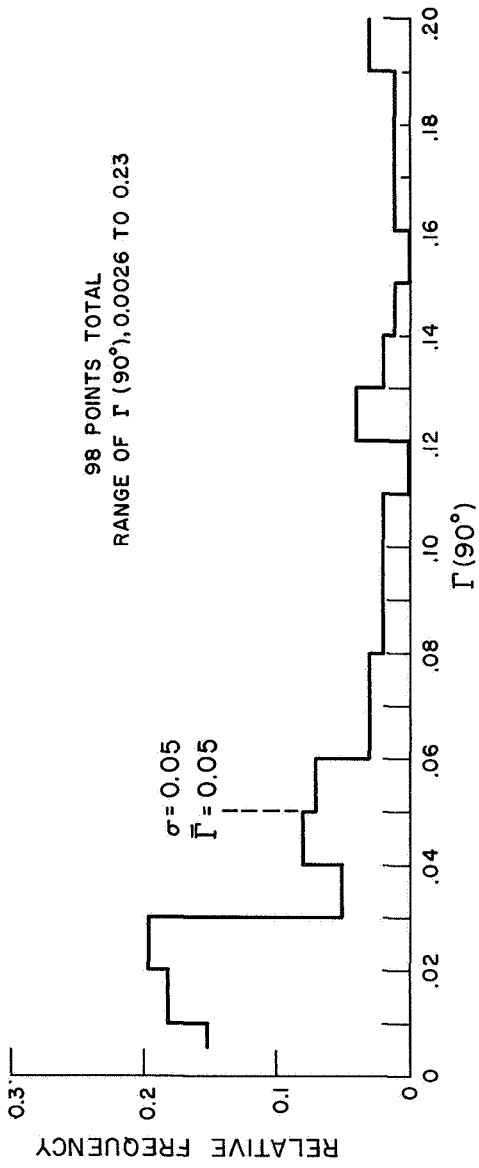

Fig. 19b Histogram of Scattering Coefficient Measurements
Idaho Falls, Idaho (Lava Beds)

APPENDIX

DESCRIPTION OF FLIGHT-TEST SYSTEM

A detailed block diagram of the radar system used in the aircraft experiment is shown in Fig. 20. All active components in the radar are solid state except for the klystron amplifier in the transmitter. The radar system requires 13 watts average power from the aircraft 28-volt supply. The klystron filament consumes 8 watts while the solid-state portion of the system requires 5 watts. The low power consumption of the solid-state equipment was achieved by using low-power circuit configurations, and by turning off most of the system during the 8 seconds between r-f bursts. The average power drawn during a 100-millisecond four-pulse burst is 45 watts.

The radar system can be classified into three basic units; transmitter, receiver, and data processor. The transmitter provides conditioned r-f power to illuminate the target so that the energy scattered back from the target area can be measured. The receiver and data processor enable the measurement of the variables required to calculate the scattering coefficient (see Section II), energy transmitted, energy received and slant range. The data processor also carries out an analog-to-digital conversion of the variables and calibration factors. The design and operation of unique units of the system are discussed in detail below.

TRANSMITTER

The transmitter consists of a light-weight klystron amplifier with associated modulator and filament circuits shown in Fig. 21. The klystron r-f input and output powers are measured by means of the calibration monitor and transmitter monitor respectively, as shown in Fig. 20.

Klystron

A standard type VA-909 klystron was modified by Varian Associates to satisfy the requirements of conduction cooling, low-weight

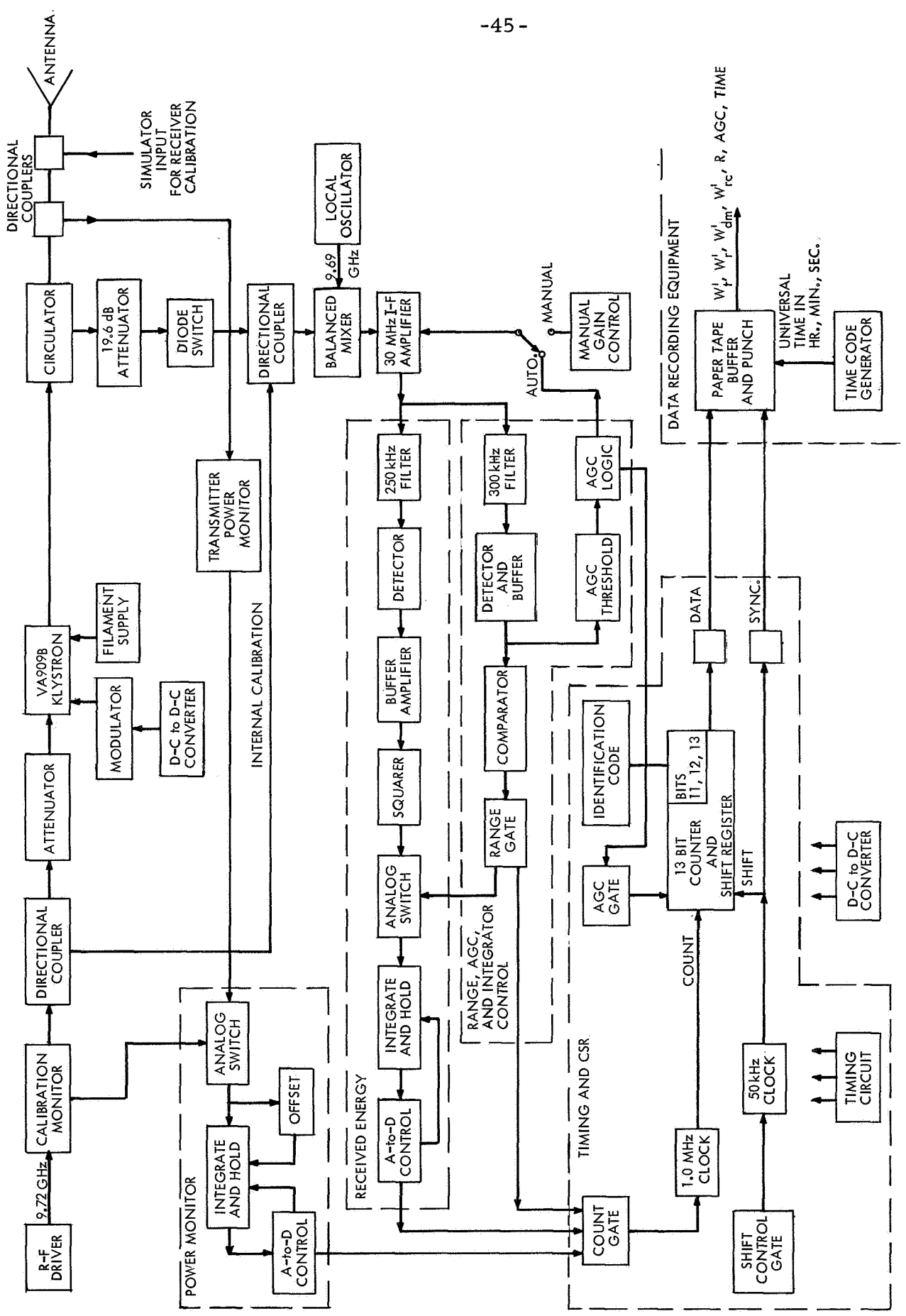

Fig. 20 Detailed Block Diagram of Radar System

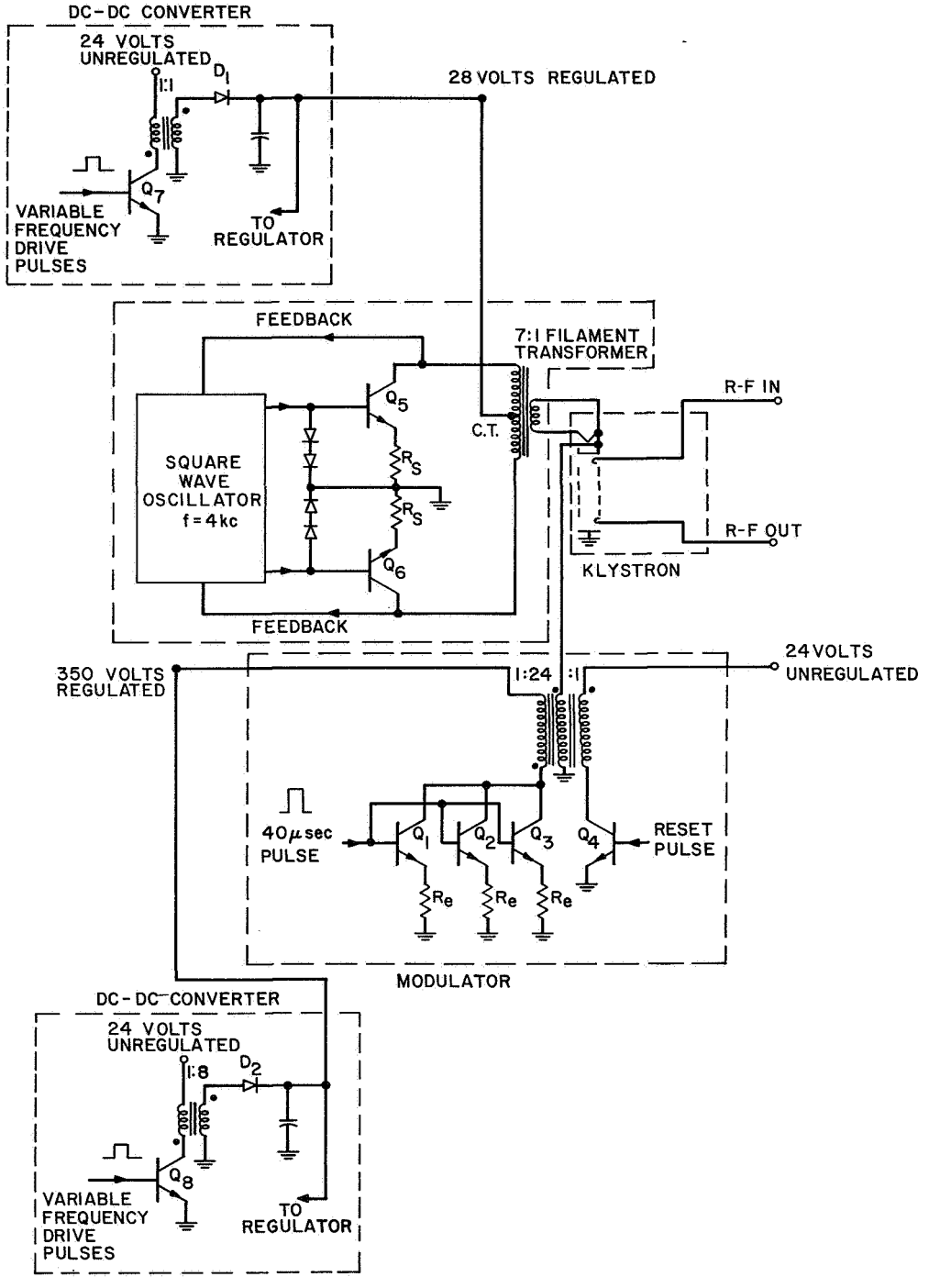

Fig. 21 Simplified Schematic Diagram of Transmitter

and low-filament power consumption.[6] Typical characteristics of the klystron designated VA-909-B are:

Power output	1 kW, peak
Duty factor	0.005
Center frequency	9.72 GHz
Tuning range	50 MHz
Gain	50 dB synchronously tuned
Beam current and voltage	650 mA at 7.5 kV
Filament power	6.5 watts
Cooling	Conduction cooled
Weight	5.5 lb.

In order to obtain the goal of 6 or 7 watts filament power, an oxide-type cathode was used. A new technique, intended to reduce the effect of ion bombardment, was utilized because oxide cathodes operating at long pulse widths are susceptible to effects of ion bombardment. However, during approximately 100 hours of operation, peak-power output gradually decreased and leveled off at 500 watts. Varian determined that the cathode emission was low and the cathode was replaced under warranty.

Modulator

The high-voltage pulse for the klystron is supplied by the secondary of a step-up transformer whose primary is switched by three high-voltage transistors in parallel. The resistors R_e in the emitters of the high-voltage transistors Q_1, Q_2 and Q_3, ensure that the current in the transistors are equal. The high-voltage transformer is reset through a third winding by transistor Q_4 in order to achieve a lower weight and size for the transformer. There is also protective circuitry, not shown in the modulator diagram, which protects the high-voltage transistors in the event of arc over in the klystron.

Klystron Filament Supply

The klystron filament power is supplied from a chopper-type circuit consisting of a square-wave oscillator, power transistors Q_5 and Q_6 and a low-capacitance isolation transformer. Use of a regulated voltage on the primary of the filament transformer results in a

regulated square-wave voltage at the filaments. Resistors R_s in the emitters of Q_5 and Q_6 automatically limit the starting surge current to the filaments. The feedback from the collectors of Q_5 and Q_6 adjusts the square-wave oscillator so that a symmetrical square wave is switched through each half of the center-tapped transformer primary.

The regulated +28 and +350 voltages are supplied by variable frequency flyback type d-c to d-c converters. Constant pulsewidth, variable-frequency pulses are applied to the base of Q_7 or Q_8, in order to produce linear current increase in the primary magnetizing inductance. When the transistors are switched off, the energy stored in the primary inductance is transferred through diodes D_1 or D_2 to the capacitors in the secondary circuit of the transformer. This type of converter has the advantage of low weight, low stand-by power requirements and a typical efficiency of over 80 percent.[7]

Power-Monitor Channels

The requirement that the transmitted energy and receiver gain stability be known to calculate the scattering coefficient (Eqs. 1-3) requires the use of two power-monitor channels.

The transmitter energy channel consists of a calibrated directional coupler, located in the r-f line preceding the antenna, which furnishes a sample of transmitted power to a calibrated diode detector. The r-f power used to monitor the gain stability of the receiving channel is obtained by extracting a portion of the r-f driver output through calibrated directional couplers and inserting the power into the mixer at the conclusion of echo pulse reception. The r-f driver output is also monitored by means of a calibrated detector.

Each power-monitor diode, described in Section IV on system calibration, provides an output voltage that is related to the r-f power incident on the monitor diode as follows:

$$v_o(t) = mp(t) + v_o \qquad (6)$$

The calibration constants m and v_o are determined as described in Section IV.

A dual-input analog switch is controlled by the timing circuits to connect the proper power-monitor input to the integrator during the calibration times. When the voltage at the input to the gated integrator reaches a level determined by the constant v_o in Eq. 6, the offset threshold detector turns on the gated integrator and connects an offset current, proportional to v_o, to the input of the integrator. The offset current effectively subtracts the constant v_o from the calibration signal so that the output of the gated integrator is proportional to calibration-signal energy. At the end of the transmitter calibration pulse, the gated integrator switches to a HOLD mode, and the voltage is A-to-D converted in the same manner as described later for the signal energy channel.

RECEIVER

The receiver used during the flight test is designed to have a degree of gain stability commensurate with an overall measurement accuracy of the total energy in the backscattered signal to ± 1 dB. As shown in Fig. 20, the receiver consists of a balanced mixer, local oscillator and 30-MHz intermediate-frequency amplifier.

Microwave Components

During the flight tests of the radar, the receiver was coupled to the antenna through a circulator, diode switch and 19.6-dB attenuator. The circulator and diode switch serve their usual functions of duplexing and receiver front-end protection. The attenuator was necessary to bring the power level of the backscattered signal within the dynamic range of the receiver, approximately -102 dBm to -60 dBm. The attenuator was used because the transmitter was operated at a power level sufficient for a range of approximately 100 miles, while the range during the flight test was about seven miles.

The local-oscillator signal is supplied by a varactor frequency-multiplier chain driven by a stable crystal oscillator. The amplitude and frequency stability of the local-oscillator signal help to minimize variations in conversion loss in the balanced mixer.

I-F Amplifier

A special i-f amplifier was designed to meet the gain-stability requirements of this experiment. A summary of the specifications of the i-f amplifier is given below and a block diagram of the amplifier is shown in Fig. 22.

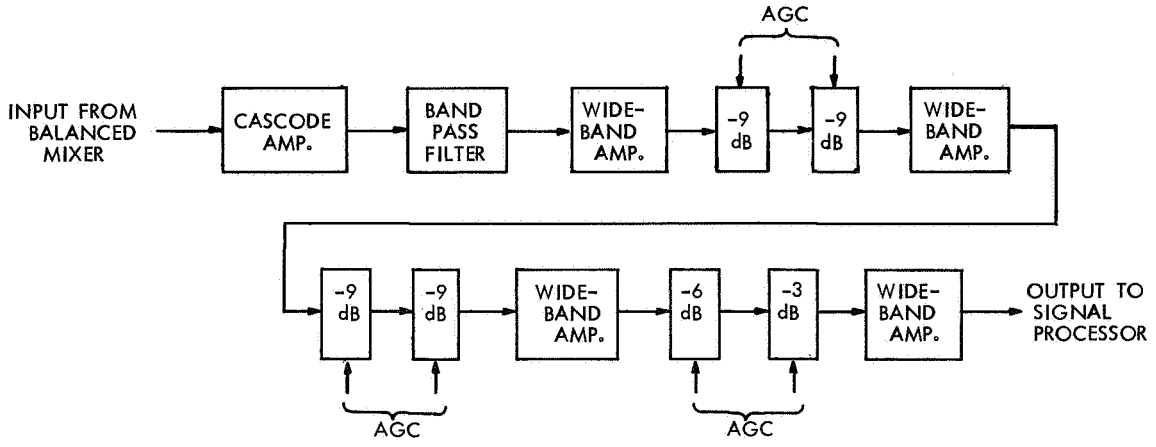

Fig. 22 Block Diagram of i-f Amplifier

Center frequency	30 MHz
3-dB bandwidth	3 MHz
Power gain	110 dB
Noise figure	3 dB
Gain control	Digital: -42 dB in 14 steps -3 dB each
Gain stability, at 110 dB Gain	± 1/2 dB, 10°C to 40°C
Gain resetability	Limited only by overall gain stability

Each stage of the i-f amplifier is designed to have a high degree of gain stability. The gain of the first stage, a tuned cascode amplifier, is held constant by the regulated bias voltages that supply all five stages in the i-f amplifier. The next four stages are untuned wide-band amplifiers and are gain-stabilized by negative feedback.

The wide-band amplifiers are coupled through electronically switched resistive attenuators that are used to control the overall gain of the i-f amplifier. A schematic diagram and description of the

wideband amplifier and attenuator circuits are presented later. The attenuators are controlled by the AGC-threshold detector and logic circuitry in the data processor in order to maintain the signal voltage below the saturation level of the squarer in the signal-energy channel. The i-f amplifier gain is adjustable in 14 steps of -3 dB each to provide a total range of -42 dB. A manually switched mode of gain control is provided for calibration and test purposes. The overall receiver gain is calibrated over the dynamic range of each gain step as described in Section IV on system calibration.

The automatic-gain control is designed to operate on the echo signal from the first transmitted pulse in each burst of four pulses and then to hold the same gain setting during the remaining three echos. During the flight test it was found that the amplitude variation among the four pulses within a burst was too great for satisfactory AGC operation, so the manual gain control was used.

A schematic diagram of the last two wideband amplifier stages and associated gain control attenuators is shown in Fig. 23. The operation of the amplifiers and attenuators is described below.

The wideband amplifier that comprises stage four in Fig. 23 is made up of transistors Q_{13}, Q_{14} and Q_{15}. The basic configuration is a direct coupled cascade of two common emitter amplifiers, Q_{13} and Q_{14} with an emitter follower Q_{15} to provide a low output impedance. The voltage gain of the amplifier is determined primarily by negative feedback, and is therefore relatively insensitive to changes in transistor parameters caused by temperature variations or changes in the power supply voltages. The negative feedback is applied between the output and the emitter of the input transistor by resistors R_1 and R_2. The power gain per stage is approximately 20 dB.

The output of the fourth stage is coupled to the final wideband amplifier through the -3 dB and -6 dB gain control attenuator network. The attenuator consists of resistors R_3, R_4 and R_5 and switching transistors Q_{16} and Q_{17}. Capacitors C_3 and C_4 decouple the attenuator from the d-c bias of the amplifiers. The switching transistors are controlled by logic in the data processor and have two states: OFF, with zero base current, ON with the base-to-emitter junction forward biased. When both transistors are OFF, the

interstage attenuation is determined by the ratio of R_3 to the 2-kΩ input impedance (Z_{in}) of the final amplifier stage, and is -1.2 dB.

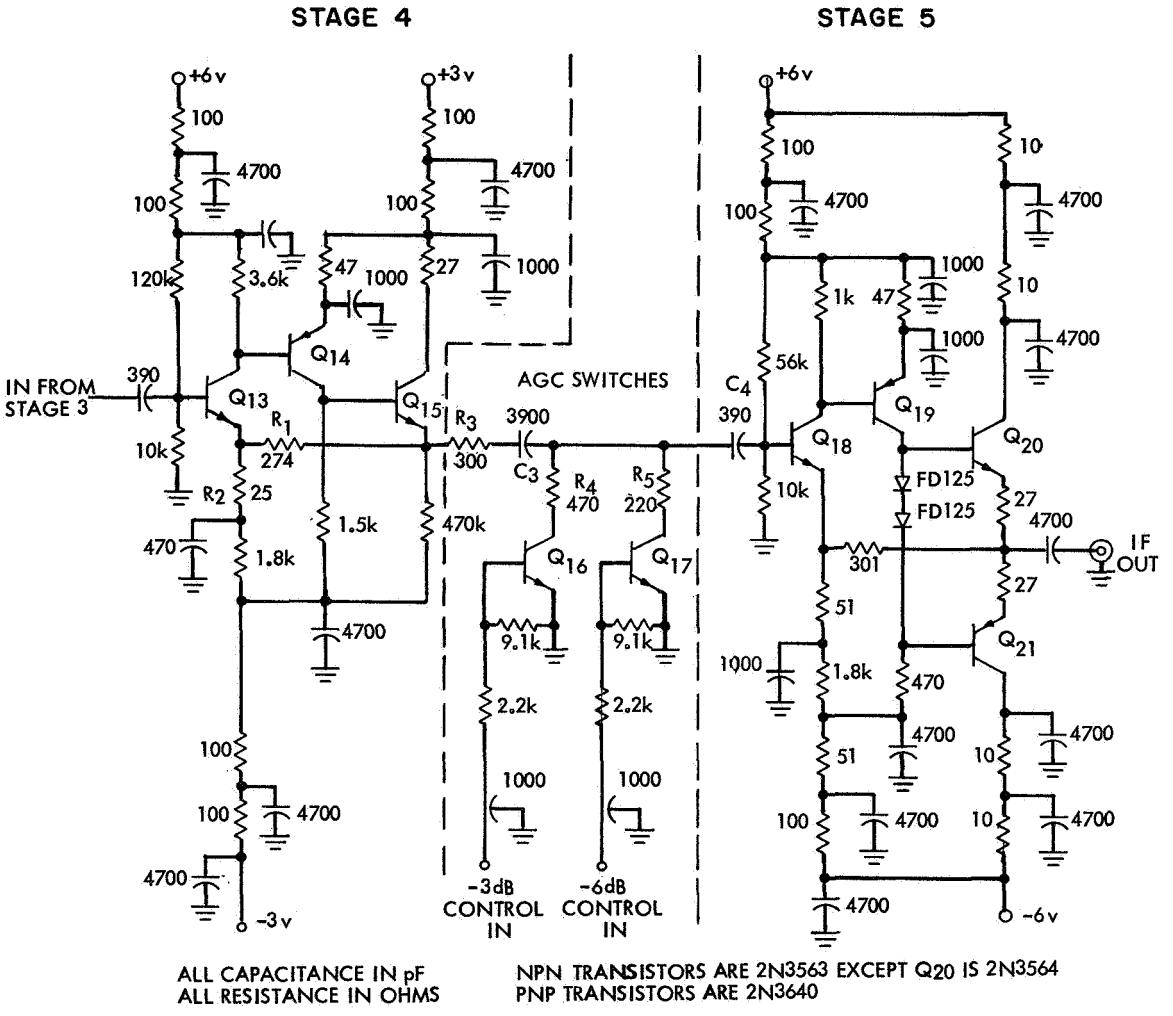

Fig. 23 Schematic Diagram of Last Two Stages of i-f Amplifier

When either Q_{16} or Q_{17} is saturated, the attenuation can be approximated as

$$Q_{16}\ \text{"ON"}\ ,\ A_{(-3dB)} = \left[20 \log \frac{R_4 \| Z_{in}}{R_4 \| Z_{in} + R_3}\right] - 1.2\ \text{dB} \qquad (7)$$

$$Q_{17}\ \text{"ON"}\ ,\ A_{(-6dB)} = \left[20 \log \frac{R_5 \| Z_{in}}{R_5 \| Z_{in} + R_3}\right] - 1.2\ \text{dB} \qquad (8)$$

The impedance of the ON transistor is much less than R_4 or R_5 at 30 MHz and can be neglected.

The final wideband amplifier stage is a modified version of stage four. Because the i-f amplifier must be capable of driving a 50-ohm terminated transmission line to +10 dBm with low distortion, a complimentary emitter follower (Q_{20}, Q_{21}) is used as the last stage of the final amplifier. The complimentary emitter follower is biased for class AB operation to reduce the standby power requirements without sacrificing maximum output power.

DATA PROCESSOR

The data processor performs several functions. It conditions the receiver i-f amplifier output signal and a sample of the transmitter-pulse energy so as to permit calculation of scattering coefficient; it provides for measurement of slant range from radar instrument to scattering surface; and it performs an analog-to-digital conversion of these three quantities so that they may be stored in digital form at the instrument location. The various circuits are discussed below.

Receiver-Signal Channel

The output of the receiver i-f amplifier is connected to two band-pass filters and envelope detectors. One filter and detector (250-kHz bandwidth) drives the received-energy channel, and the other (300-kHz bandwidth) drives the signal comparator and AGC threshold detector. The two independent filters and detectors were used to provide flexibility in choosing the bandwidth of the energy-channel filter without affecting the accuracy of the range measurement, which is dependent on the bandwidth of the threshold channel filter.

Envelope Detector. The envelope detectors are active circuits that simulate the characteristics of an ideal diode. They are linear over a range of 30 mV to 2 volts, peak to peak, and approximate the characteristic of an ideal linear detector. The circuit is unique in that it has a very low detection threshold of 10 mV peak compared with the approximately 500 mV peak threshold of a silicon diode. The detector has a dynamic range of 100 to 1 peak to peak, (10 mV to 1 V).

The detector circuit is basically a wideband operational amplifier connected in a special voltage-follower configuration. A schematic of the circuit is shown in Fig. 24. The basic operational amplifier is

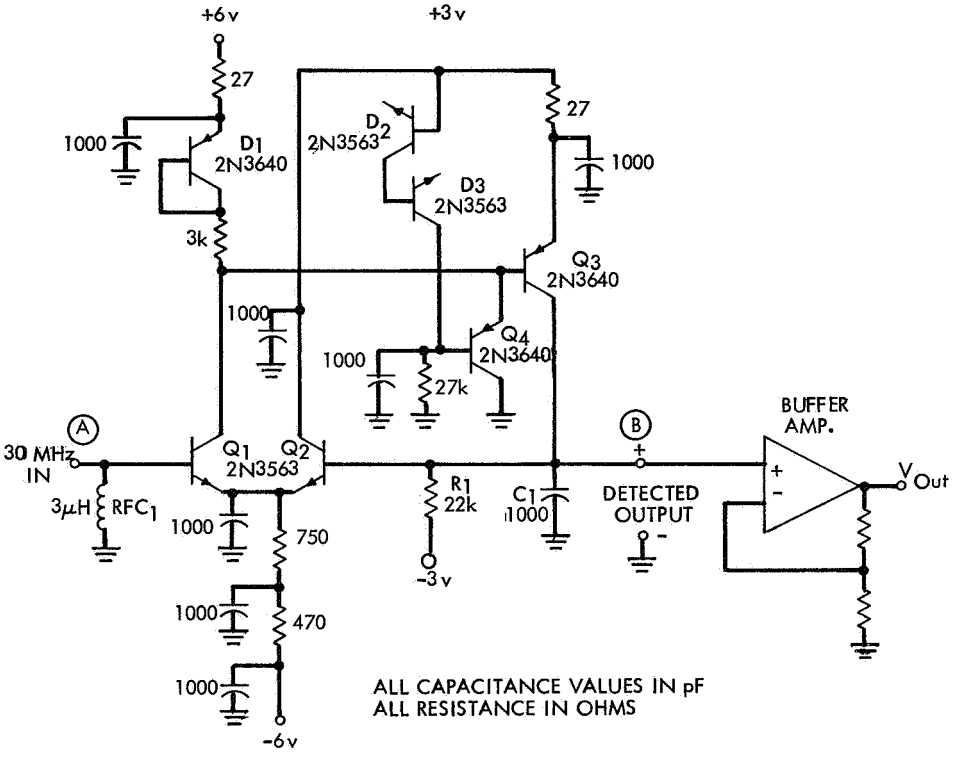

Fig. 24 Schematic Diagram of Envelope Detector

composed of a current-mode differential amplifier Q_1 and Q_2 and a common-emitter output amplifier Q_3. The network consisting of D_1, D_2, D_3 and Q_4 decreases the response time of the amplifier by limiting the positive excursion of the collector voltage of Q_1. The output of the amplifier, the collector of Q_3, is connected to the inverting output, the base of Q_2, and also to a resistor R_1 and capacitor C_1. The output will be at zero volts before a 30-MHz signal is applied to the input because the input, the base of Q_1, is held at zero volts by RFC_1. When a 30-MHz signal is applied to the input, the differential pair Q_1 and Q_2 will amplify the difference between the input voltage and the output voltage across C_1. The output amplifier Q_3 amplifies the variations in the collector current of Q_1.

During the positive peaks of the 30-MHz input, the collector current of Q_3 will charge capacitor C_1 toward the level of the positive peaks. During the time the input is negative, or less than the voltage already present across C_1, the collector current of Q_3 is reduced to zero and the output voltage decreases at a rate of $-3/R_1C_1$ volts/sec, the units of R_1 and C_1 being chosen so that their product is measured in seconds. Since the discharge rate $-3/R_1C_1$ (volt/sec) is much slower than the charge rate $^{i}Q_3/C_1$, the voltage across C_1 will follow the envelope of the positive peaks of the 30-MHz input.

Comparator and Range Gate. The comparator, which is connected to the detected output of the 300-kHz filter, operates in conjunction with the range gate to control the gated integrator in the signal-energy channel and the range time clock. The comparator compares a "long time" average ($T >> 1/B$, $B = 300$ kHz) to a "short time" average ($T > 1/B$) of the output voltage of the 300-kHz filter and detector. The ratio of "short time" to "long time" amplitudes was chosen to give a false-alarm rate less than one per second. When the "short time" average exceeds the "long time" average by the preset factor, the output of the comparator changes state, indicating a tentative identification of an echo signal. In order to further reduce the chance of a false alarm, the output of the comparator is gated with a pulse that extends from 55 μsec to 110 μsec after the leading edge of a transmitted pulse. This interval corresponds to the echo times that were possible during the aircraft flight tests.

The output of the range gate changes state only when there is a coincidence between a signal threshold event and a possible range pulse. When a echo is thus detected, the range gate stops the range clock, which was started at the beginning of a transmitter pulse. The range-clock pulses are counted by the counter shift register, so that the counter contains a binary number that is linearly proportional to range time (or distance) when the range clock is stopped. This number is shifted out and recorded on paper tape.

Gated Signal Integrator. The main function of the received-energy channel is to produce a voltage that is linearly proportional to the energy in the backscattered signal. The energy W in a pulse signal is defined as

$$W = k\int_{T_1}^{T_2} v(t)^2\, dt \tag{9}$$

where
- W = pulse energy
- k = a constant
- $v(t)$ = instantaneous voltage within a echo pulse
- T_1 = start time of echo signal
- T_2 = end time of echo signal

The received-energy channel implements Eq. 9 with analog-signal-processing techniques. The output voltage of the 250-kHz filter and detector is amplified to increase its full-scale value of 10 volts. The output of the buffer amplifier is connected to a squarer that has the voltage-transfer characteristics given by Eq. 10 with an error within ±2 percent.

$$v_{out}(t) = -\frac{[v_{in}(t)]^2}{10} \tag{10}$$

$$0.2 \text{ volt} < v_{in}(t) < 10 \text{ volts}$$

Thus, the output voltage of the squarer is proportional to the power in the backscattered signal. The output of the squarer, in turn, is connected to a gated integrator, which is controlled by the range gate and the analog-to-digital converter described in later paragraphs. When an echo signal is detected, the range gate causes the gated integrator to integrate the squarer output voltage with respect to time. At the end of the echo pulse, the gated integrator is switched to a hold mode to maintain the final value of the integrated signal. The voltage held by the integrator is linearly proportional to the energy in the backscattered signal, as given by Eq. 9.

Five milliseconds after the echo signal ends, the magnitude of the voltage held by the gated integrator is converted to a 10-bit binary number. The analog-to-digital conversion is accomplished by integrating a constant current of polarity opposite to that of the signal and counting the number of 1-MHz clock pulses between the start of the A-to-D integration and the instant the output of the integrator reaches

zero volts. This process produces a binary number in the counter shift register that is linearly proportional to the energy in the echo signal.

The most significant feature of the gated signal integrator and associated control circuits is the high level of performance attained with an average power consumption in only 16 milliwatts. The key element in achieving the high performance of the integrator is a specially designed operational amplifier which is described in a later section. The operation of the signal integrator, which is similar to the calibration integrator, is described below, and a diagram of the integrator and associated circuits is shown in Fig. 25.

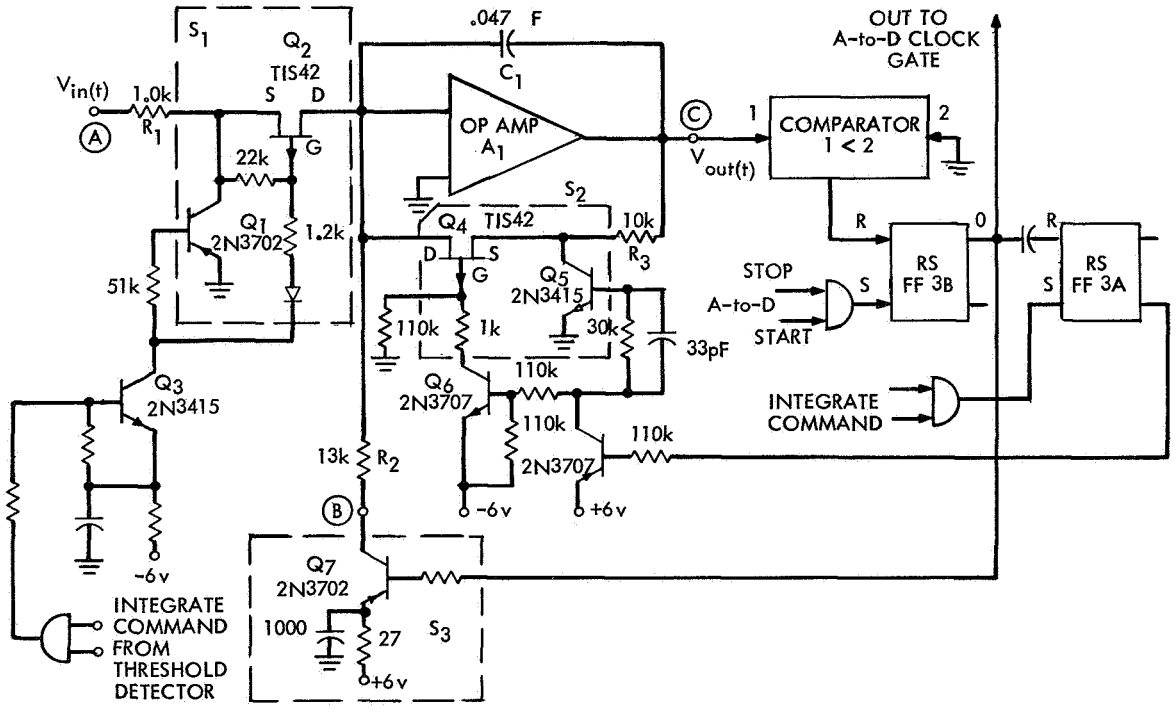

Fig. 25 Schematic Diagram of Gated Signal Integrator

The gated signal integrator performs three functions: integration of the detected and squared echo signal with respect to time, temporary storage of the integrated signal, and analog-to-digital conversion to the final value of the integrated signal. In order to carry out these functions, the integrator is sequenced through four modes of operation by the system timing circuits and the integrator control logic. The modes are:

1. Integrate the voltage at terminal A, Fig. 25.
2. Hold the final value of the integrated voltage.
3. A-to-D convert the final value by integrating constant voltage at terminal B, Fig. 25.
4. Reset and hold the voltage across the integrating capacitor C_1 to zero.

The basic integrator consists of an operational amplifier A_1 with a capacitor C_1 connected between the output and inverting input. The mode of operation is determined by the states of the analog switches connected in series with the input and in shunt with the feedback capacitor C_1. When the gated integrator receives an "integrate" command from the signal threshold-range-gate circuits, the integrator is switched from mode 4, RESET, to mode 1. This is accomplished by opening the feedback switch S_2 and closing the signal input switch S_1. The input switch is closed by cutting off transistor Q_1 and biasing the field effect transistor Q_2 to low-channel resistance. With S_2 open and S_1 closed, the output voltage of the integrator v_F is related to the input voltage at terminal A as follows:

$$v_F = -\frac{1}{R_A C_1} \int_{T_1}^{T_2} v_{in}(t)\,dt \qquad (11)$$

$$R_A = R_1 + R_{Q_1}$$

$$R_{Q_1} = \text{ON channel resistance of } Q_1$$

The time limits of the integral in Eq. 11 are determined by the signal threshold circuit, and the constant $1/R_A C_1$ forms part of the overall receiver calibration constant.

At the end of the integration time the gated integrator is switched to mode 2 HOLD by opening the input switch and maintaining switches S_2 and S_3 in their open states. With all the switches open, the output voltage of the integrator changes at a very slow rate determined by the amplifier input current and switch leakage current. During the 5-millisecond HOLD interval, the change in output voltage is less than 10 millivolts or 0.1 percent of the full-scale value of 10 volts.

The analog-to-digital conversion of the voltage held by the integrator begins when the system timing signals SET flip-flop 3B, thereby switching the operation of the integrator to mode 3. The output of flip-flop 3B turns on switch S_3 and simultaneously starts the 1-MHz A-to-D clock. Switch S_3 connects the input of the integrator through resistor R_2 to a fixed voltage of the integrator to decrease linearly with time, as shown by the equation:

$$v_{out}(t) = v_F - \frac{v_R(t-t_o)}{R_2 C_1} \qquad (12)$$

$$t > t_o \ , \ t_o = \text{A-to-D start time}$$

$$v_R = 6 \text{ volts}$$

When the integrator output voltage, $v_o(t)$ reaches zero volts, the comparator resets flip-flop 3B, which in turn resets flip-flop 3A. The control flip-flops stop the A-to-D clock, turn off S_3 and turn on the feedback switch S_2, to put the integrator in mode 4, RESET. At the end of the A-to-D conversion time, the CSR contains a number linearly proportional to the energy in the received echo signal.

Operational Amplifier. The operational amplifier used in the gated signal integrator was specially designed to have high voltage gain, low input current and offset voltage, and high peak-current output capability, with a static power consumption of only 10 milliwatts. The specifications of the amplifier are listed below and the schematic of the amplifier is shown in Fig. 26.

Specifications of Operational Amplifier

Voltage gain	10^5
Offset current at inverting input	5×10^{-8} amp
Offset voltage	0.5 mV
Offset voltage drift	5 μV/^{o}C at 20^{o}C
Output voltage	0 to +10 volts
Output current	±15 mA
Unity gain bandwidth	3 MHz
Static power consumption	10.5 mW (0.35 mA from ±15 V supplies)

The operational amplifier consists of two differential-amplifier stages, an emitter-follower buffer, and a complementary emitter-follower output stage.

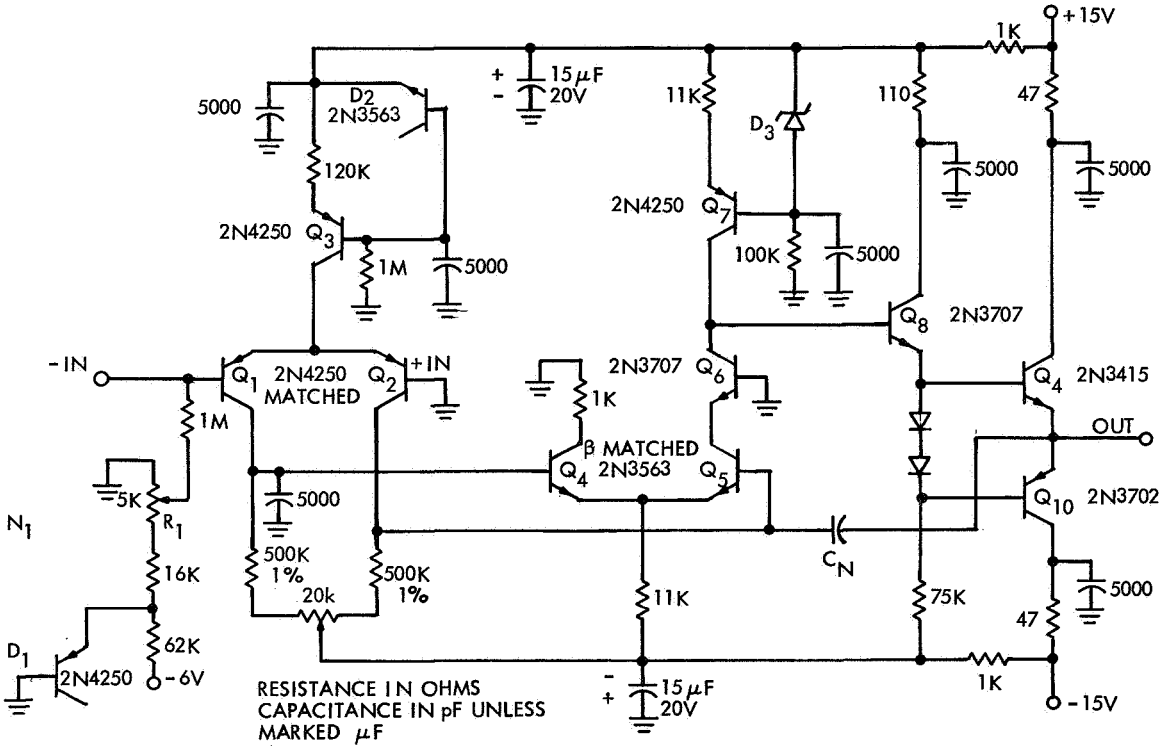

Fig. 26 Schematic Diagram of Operational Amplifier for Gated Signal Integrator

The differential input amplifier Q_1 and Q_2 is biased to provide low input current and voltage drift. The bias network connected to the base of Q_1 further reduces the current out of the inverting input to less than 50 nanoamp.

The second stage, which includes Q_4, Q_5 and Q_6, is designed to provide a high d-c voltage gain ($\sim 10^4$) and good frequency response. The cascode connection of Q_5 and Q_6 makes it possible to achieve both high gain and wide bandwidth by eliminating the effects of degenerative feedback in the transistors. The collector current for Q_6 is supplied by a constant-current source Q_7 and its associated circuitry. The current source provides a high-resistance ($\sim 10^7$ ohms) collector load for Q_6 and thus maximizes the direct-voltage gain of the cascode. The low voltage drop across the current source (3 volts)

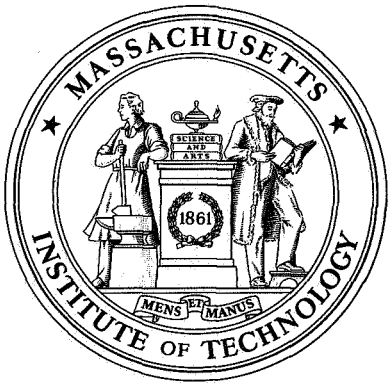
MASSACHUSETTS
INSTITUTE OF TECHNOLOGY
SCIENCE AND ARTS
1861
MENS ET MANUS